Optimization of Yb^+ fluorescence and hyperfine-qubit detection

S. Ejtemaee, R. Thomas, and P. C. Haljan
Department of Physics, Simon Fraser University, 8888 University Dr., Burnaby, British Columbia, V5A 1S6 Canada
(Received 13 September 2010; published 29 December 2010)

Fluorescence of single, trapped $^{171}Yb^+$ ions has been experimentally studied as a function of laser polarization, power, and detuning and as a function of magnetic field strength. The suppression of efficient fluorescence by coherent population trapping and the counteracting effect of the magnetic field are found to agree with theoretical predictions. For comparison, a fluorescence study has also been made of the isotope $^{174}Yb^+$ for which coherent population trapping is absent on the main fluorescence and laser cooling transition. Finally, state-sensitive fluorescence detection of the $^{171}Yb^+$ hyperfine qubit is studied, including the role of coherent population trapping in the optimization of detection parameters. A qubit detection fidelity of greater than 97% is achieved.

DOI: 10.1103/PhysRevA.82.063419 PACS number(s): 32.60.+i, 32.10.Fn, 03.67.Lx

I. INTRODUCTION

Laser-cooled, trapped $^{171}Yb^+$ ions currently find application in precision spectroscopy for time and frequency metrology [1–4], ion-trap quantum information processing [5–8], and studies of interactions with ultracold atoms [9,10]. In these applications, efficient fluorescence scattering is required as it forms the basis for the mechanical action of Doppler laser cooling [11] and permits high-fidelity state-selective detection, for example, of hyperfine qubits [12,13]. Due to the multilevel nature of atomic systems in general, efficient fluorescence can be compromised by optical pumping to dark states. In most cases, this is simply countered through additional laser repump frequencies or by the appropriate choice of laser polarizations to ensure a closed fluorescence cycle. However, if two or more lower states share an excited state, interference effects can arise such that, even though all couplings are present, the fluorescence will be suppressed through coherent population trapping [14,15]. In this case the atom or ion is optically pumped into a dark state composed of a superposition of lower states.

Coherent population trapping and its related physics [16] is commonly discussed for a pair of laser beams applied to a three-level Λ system and can be exploited for useful applications including novel cooling schemes [17,18]. However, coherent population trapping can also arise in a Zeeman-degenerate transition driven by a single laser field and leads to a detrimental suppression of fluorescence. One particular case is a transition with higher multiplicity in the ground state, which occurs for the hyperfine $^2S_{1/2}(F=1)-{}^2P_{1/2}(F=0)$ fluorescence and cooling transition in $^{171}Yb^+$ as well as $^{199}Hg^+$. The cooling and repump transitions for several other ion species are also susceptible. In the limit of no magnetic field, the coherent population trapping effect can be interpreted as optical pumping to polarization dark states in the absence of a well-defined quantization axis [19]. The problem persists, however, at finite magnetic fields for sufficiently strong laser power. Berkeland and Boshier [20] have provided a detailed theory of dark-state formation in Zeeman-degenerate systems and have described the two common experimental methods for dark-state destabilization. The first method involves modulating the polarization of the laser at a rate sufficiently fast that the ground-state populations and coherences cannot follow, effectively projecting out of the dark state [19,21]. The second method uses a magnetic field to rotate the ground-state spin-polarization out of the dark state by magnetic field precession [22–24]. The laser modulation scheme has the advantage that it works near zero magnetic field where, for example, clock-state hyperfine qubits [12] of the type in $^{171}Yb^+$ are first-order insensitive to field fluctuations. The advantage of the magnetic field method is that it is simple to implement.

In this experiment we study in detail the magnetic field method of dark-state destabilization for single, trapped $^{171}Yb^+$ ions, which we intend for use as hyperfine qubits, and compare our results with the theory derived by Berkeland and Boshier. We also study the fluorescence behavior of the $^{174}Yb^+$ isotope, chosen as a "control" ion for comparison since it is free of hyperfine structure and does not have coherent population trapping on its main fluorescence transition. Fluorescence is studied as a function of magnetic field, laser power, polarization, and detuning. These parameters are all calibrated *in situ*, with the exception of laser power, and at reasonably low error to suppress the effect of parameter correlations in fits to theory. Finally, building on our studies of fluorescence, we investigate the detection of the $^{171}Yb^+$ hyperfine qubit and the role played by coherent population trapping in optimizing the detection parameters. Although the details will differ, a similar procedure should extend to other ion species with larger hyperfine spins as long a control isotope is readily available such as $^{40}Ca^+$ for $^{43}Ca^+$ and $^{138}Ba^+$ for $^{137}Ba^+$.

II. THEORY

The relevant level structure of $^{171}Yb^+$ with nuclear spin 1/2 and $^{174}Yb^+$ is shown in Fig. 1. The $6s^2S_{1/2}$-$6p^2P_{1/2}$ transition at 369.52 nm is the primary transition used for laser cooling and fluorescence detection and has a natural linewidth $\gamma/2\pi = 19.60(5)$ MHz inferred from previous lifetime measurements [25,26]. A small leak from the $^2P_{1/2}$ excited state to the low-lying $^2D_{3/2}$ state occurs with a branching ratio $\alpha = 0.005\,01(15)$ [8] and requires a repump laser to maintain fluorescence. Clear-out of the $^2D_{3/2}$ state is done via a 935.2-nm transition to the $^3D[3/2]_{1/2}$ excited state. The 935.2-nm transition has a linewidth of $\gamma_{IR}/2\pi = 4.22(6)$ MHz inferred from previous lifetime measurements [27] and returns to the ground state with a calculated branching ratio

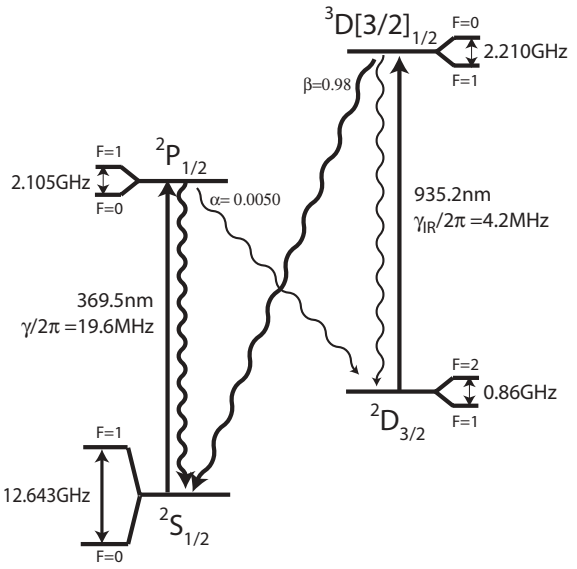

FIG. 1. Basic Yb^+ atomic structure involved in fluorescence detection and cooling, including branching ratios α and β. Hyperfine states for $^{171}Yb^+$ (nuclear spin $I = 1/2$) are also shown. Additional low-lying $^2D_{5/2}$ and $^2F_{7/2}$ states have been omitted for clarity.

$\beta = 0.982$ [28]. We assume that the remainder of the branching ratio is back to the $^2D_{3/2}$ state. We ignore the 52 ms lifetime of the metastable $^2D_{3/2}$ state [29] in our fluorescence calculations since it is long compared to the other time scales of photon-scattering processes considered here. There is also a low-lying and long-lived metastable $^2F_{7/2}$ state, not shown in Fig. 1, that is not strongly linked to the $^2D_{3/2}$ state because of selection rules but nevertheless can be populated via collisional processes [30–32]. While an additional repump laser at 638.6 nm is necessary to depopulate the $^2F_{7/2}$ state, collisional deexcitation events are relatively rare in practice and so we ignore the $^2F_{7/2}$ state in our model of fluorescence. Although the $^{171}Yb^+$ hyperfine splittings used in our calculations, and indicated in Fig. 1, have been previously measured—see, for example, Ref. [8]—we have reconfirmed most of them in the process of optimizing our setup.

The ion's UV fluorescence rate $\eta\gamma\mathcal{P}_p$ that we measure experimentally is proportional to the photon collection efficiency η of our imaging system and proportional to the total $^2P_{1/2}$ excited-state population $\mathcal{P}_p$. To calculate this and other state populations as well as coherences, we calculate the steady-state solution for the density matrix of ion internal states from the Liouville equation,

$$i\hbar\frac{d\rho_{kl}}{dt} = [H,\rho]_{kl} + i\hbar\langle k|\Gamma\rho|l\rangle, \tag{1}$$

where ρ_{kl} represents the density matrix, H includes the Hamiltonian for the atom's interaction with an external magnetic field and various laser electric fields, and the last damping term accounts for spontaneous emission [33]. We ignore any effect of ion motion and assume a laser linewidth much narrower than the natural linewidth.

It is long but straightforward to account for the complete set of levels involved in fluorescence; however, the problem can be solved in a modular fashion. Since the leakage rate to the $^2D_{3/2}$ state is weak, the essential steady state fluorescence behavior is accounted for by the $^2S_{1/2}$-$^2P_{1/2}$ transition, with only a small correction required for the $^2D_{3/2}$ repump as long as the 935.2-nm laser parameters are properly optimized. Figure 2 shows the Zeeman-resolved level structure of the $^2S_{1/2}$-$^2P_{1/2}$ transition for each of the isotopes, the detailed solutions for which are discussed separately in the following.

A. $^{171}Yb^+$

Doppler cooling and fluorescence for $^{171}Yb^+$ works on the $^2S_{1/2}(F = 1) \rightarrow {}^2P_{1/2}(F = 0)$ transition [Fig. 2(a)], which is closed to the $^2S_{1/2}(F = 0)$ ground state except via weak off-resonant leakage under typical circumstances. For steady-state fluorescence and Doppler cooling, the weak optical pumping to $^2S_{1/2}(F = 0)$ is countered by an additional repump laser [Fig. 2(a)]. If the repump is sufficiently strong, then the net effect is a negligible correction to overall fluorescence below 1% which we ignore. Thus, we can isolate the $F = 1$ to $F = 0$

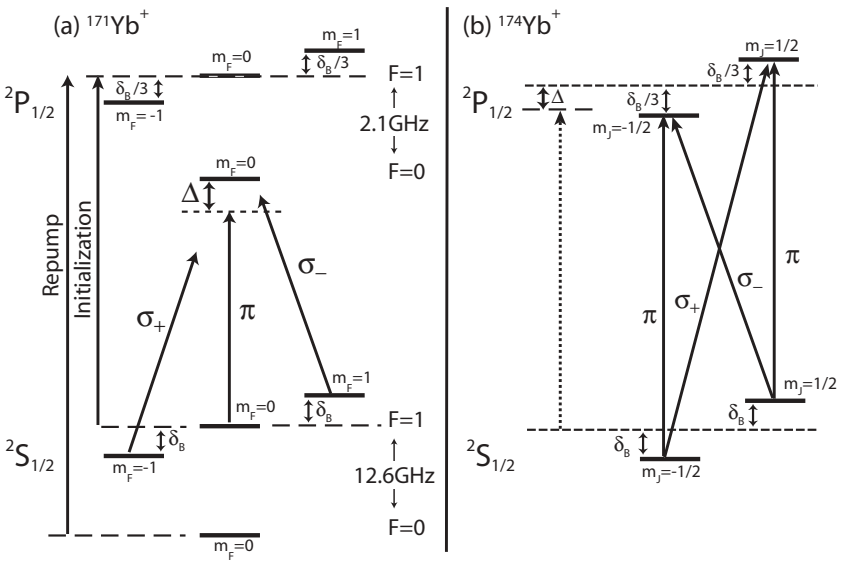

FIG. 2. Zeeman resolved structure of primary $^2S_{1/2}$-$^2P_{1/2}$ transition for (a) $^{171}Yb^+$ and (b) $^{174}Yb^+$. Zeeman splittings due to magnetic field B are indicated in terms of $\delta_B = \mu_B B/\hbar$. Laser detuning Δ is defined relative to the $B = 0$ transitions as shown. The polarization-resolved branching ratios for $^{171}Yb^+$ are all 1/3 while those for $^{174}Yb^+$ are 1/3 and 2/3 for π and σ transitions respectively. The UV hyperfine repump transition and the optical pumping transition used for qubit initialization to $^2S_{1/2}|F = 0, m_F = 0\rangle$ are also shown for the case of $^{171}Yb^+$.

transition in lowest order. Assuming a linearly polarized laser field, which is the only case considered in this work, the steady-state solution for the $|^2P_{1/2}; F = 0, m_F = 0\rangle$ excited state's population $\mathcal{P}_{p0}$, quoted with modification from Ref. [20], is

$$\mathcal{P}_{p0} = \frac{3}{4}\frac{\cos^2\theta_{BE}\sin^2\theta_{BE}}{1+3\cos^2\theta_{BE}}\frac{\frac{\Omega^2}{3}}{\Delta^2+\left(\frac{\Gamma_{171}}{2}\right)^2} \tag{2}$$

$$\left(\frac{\Gamma_{171}}{2}\right)^2 = \left(\frac{\gamma}{2}\right)^2 + \frac{\Omega^2}{3}\cos^2\theta_{BE}\frac{1-3\cos^2\theta_{BE}}{1+3\cos^2\theta_{BE}} + \frac{\cos^2\theta_{BE}}{1+3\cos^2\theta_{BE}}\left(\frac{\Omega^4}{36\delta_B^2}+4\delta_B^2\right). \tag{3}$$

In this equation, γ is the natural linewidth of the transition and $\delta_B = \mu_B B$ is the Zeeman shift between sublevels in the $F = 1$ ground-state due to magnetic field B. The laser's detuning Δ is referenced from the transition at $B = 0$, while θ_{BE} is the angle between laser's electric field and the external magnetic field. Finally, Ω is the laser Rabi frequency, which is a function of laser power or intensity I. The Rabi frequency and associated on-resonant saturation parameter s_0 are defined as follows in terms of the bare $^2S_{1/2}$-$^2P_{1/2}$ fine-structure transition to make comparison between $^{171}Yb^+$ and $^{174}Yb^+$ explicit:

$$\Omega \equiv \sqrt{\frac{s_0}{2}}\gamma \quad s_0 = \frac{I}{I_{\text{sat}}} \quad I_{\text{sat}} = \frac{\pi hc}{3\lambda^3}\gamma. \tag{4}$$

The saturation intensity $I_{\text{sat}} = 51\ \text{mW/cm}^2$ as defined is a function of the $^2S_{1/2}$-$^2P_{1/2}$ linewidth and wavelength only, which are the same for $^{171}Yb^+$ and $^{174}Yb^+$ to a very good approximation. Note that the actual saturation intensity, which also depends on coupling coefficients, will be substantially larger than I_{sat} due to the multiplicity of states involved in the transition.

From Eq. (2) it can be seen that $^{171}Yb^+$ has polarization dark states for $\theta_{BE} = 0^\circ$ and $\theta_{BE} = 90^\circ$, which correspond to situations where at least one of the three polarization couplings in Fig. 2(a) vanishes. Since all the couplings have the same Clebsch-Gordon magnitude, the optimum excited-state population at fixed δ_B is achieved when the Rabi frequencies for the three polarization components are *approximately* all equal [34]. This occurs at a linear laser polarization given by $\theta_{BE} \approx \theta_o \equiv \arccos(\frac{1}{\sqrt{3}}) = 54.7^\circ$. The excited state population on resonance in this case reduces to the simple value $\Omega^2/9\Gamma_{171}^2$.

Even when all couplings are present, the higher multiplicity in the $F = 1$ ground state of the transition can still lead to suppressed fluorescence through coherent population trapping. The ion is pumped into a ground-state spin coherence that is decoupled from the laser field. A sufficiently strong magnetic field destabilizes the spin coherence by introducing rapid time-dependent phases to the Zeeman levels. As discussed in Ref. [20], the Ω^4/δ_B^2 term in the effective linewidth [Eq. (3)] describes the competition between the magnetic-field–induced evolution of the dark states and the ability of the dressed atom to follow.

At low laser powers the linewidth is roughly constant and the excited-state population grows as $\mathcal{P}_{p0} \sim \Omega^2$ while at high powers ($\Omega \gg \gamma, \delta_B$) the effective linewidth broadens rapidly and the population drops off as $\mathcal{P}_{p0} \sim 1/\Omega^2$. With the approximation $\theta = \theta_0$, at fixed δ_B the fluorescence peaks at the following Rabi frequency

$$\Omega_{pk} \approx \left[\frac{9\delta_B^2}{2}\left(3\gamma^2+12\Delta^2+8\delta_B^2\right)\right]^{1/4}, \tag{5}$$

where the peak excited-state population is

$$\max(\mathcal{P}_{p0}) \approx \frac{1}{\sqrt{2}}\frac{\delta_B}{\sqrt{3\gamma^2+12\Delta^2+8\delta_B^2}}. \tag{6}$$

In the limit of large magnetic field and laser power, the excited-state fraction can reach 1/4, half of the standard saturation value.

The excited state's population in Eq. (2) can be generalized to the following form to account for the decay from $^2P_{1/2}(F = 0)$ state to the low-lying $^2D_{3/2}(F = 1)$ state, as well as the countereffect of a 935.2-nm laser repumping via the $^3D[3/2]_{1/2}(F = 0)$ state:

$$P_{p0}^{(r)} = \frac{\mathcal{P}_{p0}(\alpha = 0)}{1+\xi\mathcal{P}_{p0}(\alpha = 0)}. \tag{7}$$

The repump factor ξ is defined as

$$\xi = \frac{\alpha\gamma}{\beta\gamma_{1R}}\frac{1}{\mathcal{P}_{[3/2]}(\beta = 0)}. \tag{8}$$

Besides the linewidths and branching ratios already defined (Fig. 1), $\mathcal{P}_{p0}(\alpha = 0)$ is the $^2P_{1/2}(F = 0)$ population assuming no leakage to the $^2D_{3/2}(F = 1)$ state and is given by Eq. (2), while $\mathcal{P}_{[3/2]}(\beta = 0)$ is the $^3D[3/2]_{1/2}(F = 0)$ excited-state population assuming a closed 935.2-nm transition.

The 935.2-nm repump transition $^2D_{3/2}(F = 1) \rightarrow {}^3D[3/2]_{1/2}(F = 0)$ itself is susceptible to coherent population trapping. Since the hyperfine structure is the same as the UV transition, Eq. (2) can be applied to calculate $\mathcal{P}_{[3/2]}(\beta = 0)$ also. Over the range of magnetic field 3.4–8.1 G where most of the data for this experiment are taken, near-optimal polarization and power of the 935.2-nm laser give values of ξ that correspond to a maximum correction to the UV fluorescence of below 2%. This correction is relatively small; however, the effect of the repump transition is experimentally significant for the $^{174}Yb^+$ ion, which reaches much higher $^2P_{1/2}$ excitation values, and so we include the correction for both isotopes.

As a final note, the $^2D_{3/2}(F = 2)$ state in $^{171}Yb^+$ has been ignored since it is approximately closed to the fluorescence cycle and is only populated weakly. The state *is* cleared out in the experiment using another repump laser frequency but this does not constitute a significant correction to the fluorescence theory for our purposes.

B. $^{174}Yb^+$

The same procedure used to calculate the steady-state UV fluorescence of $^{171}Yb^+$ from the Liouville equation can be applied to $^{174}Yb^+$. The problem is simpler for $^{174}Yb^+$ in that it has no hyperfine structure, and there is no coherent population trapping for its $^2S_{1/2}$-$^2P_{1/2}$ transition [20]. However, solving the steady-state solution for $^{174}Yb^+$ analytically is in some sense more difficult because of the appearance in the Liouville equation of terms describing the decay of excited-state

coherences to those in the ground state. Numerical simulations, though, indicate that the coherences between excited-state Zeeman levels and those between ground-state levels are zero or close to it over a wide range of parameters, so we set them to zero in our equations and proceed with an approximate solution for steady state. This approximation amounts to a rate-equation approach.

The analytical solutions for the rate equations, in particular the total $^2P_{1/2}$ population, are still too involved but can be further approximated as long as the magnetic field is not too large ($\delta_B \lesssim \gamma/2$). To a good approximation theoretically, we find that the excited-state population can be simplified as follows to a saturation form analogous to a two-level system with an effective linewidth extracted from the $\Delta \to \infty$ limit:

$$\mathcal{P}_p = \sum_{M_J=-1/2}^{1/2} \mathcal{P}_p(M_J) = \frac{1}{2}\frac{\frac{\Omega^2}{6}}{\Delta^2 + \left(\frac{\Gamma_{174}}{2}\right)^2} \tag{9}$$

$$\left(\frac{\Gamma_{174}}{2}\right)^2 = \frac{\Omega^2}{6} + \frac{\gamma^2}{4}\frac{\left(1+\frac{16\delta_B^2}{9\gamma^2}\right)\left(1+\frac{64\delta_B^2}{9\gamma^2}\right)}{1+\frac{16\delta_B^2}{9\gamma^2}(3\cos^2\theta_{BE}+1)}. \tag{10}$$

These equations apply as before to the special case of a linearly polarized laser field. As can be seen, unlike $^{171}Yb^+$ there is no polarization dark state for $^{174}Yb^+$ at any polarization angle nor is there a coherent dark state. The effective linewidth includes both power and Zeeman broadening and approaches the natural linewidth γ in the limit of vanishing magnetic field ($\delta_B \to 0$) and laser power ($\Omega \to 0$). Peak excited-state population, and so maximum fluorescence, occurs at $\theta_{BE} = 0$, which corresponds to a π-polarized laser field.

On resonance, the excited-state population reduces to $\Omega^2/3\Gamma_{174}^2$. In the absence of Zeeman broadening, the excited state reaches half its maximum value at $s_0 = 3$, in other words at 3 times higher power than for a two-level cycling transition, because of Zeeman sublevel branching ratios.

Similar to $^{171}Yb^+$, repump effects associated with leakage to the $^2D_{3/2}$ state can be considered for $^{174}Yb^+$. As mentioned above, the correction is much more significant. Repump-corrected Eqs. (7) and (8) also apply to $^{174}Yb^+$ with $\mathcal{P}_{p0}$ replaced by $\mathcal{P}_p$ taken from Eq. (9) and $\mathcal{P}_{[3/2]}(\beta = 0)$ now identified as the total population in the two Zeeman sublevels of the excited state $^3D[3/2]_{1/2}$. The $^2D_{3/2} \to {}^3D[3/2]_{1/2}$ repump transition in $^{174}Yb^+$ is susceptible to dark-state formation, but calculating the repump factor is more challenging than for $^{171}Yb^+$ since the number of Zeeman levels involved is larger, and no obvious approximations present. Therefore, we resort to numerical simulation to estimate the value of $\mathcal{P}_{[3/2]}(\beta = 0)$ as a function of magnetic field and the 935.2-nm laser polarization and power. A repump factor of about $\xi = 0.1$ is obtained for the magnetic field range 3.4–8.1 G and near-optimal 935.2-nm laser parameters considered in this experiment. When the UV transition is saturated ($\mathcal{P}_p = 0.5$), the repump effects are expected to comprise approximately a maximum 5% correction to the fluorescence.

C. Detection fidelity for $^{171}Yb^+$ qubit

A primary practical application for studying $^{171}Yb^+$ fluorescence is to optimize the fidelity of qubit detection using state-selective fluorescence [11]. The qubit states are the ground hyperfine clock states, $|\downarrow\rangle \equiv |^2S_{1/2}; F = 0, m_F = 0\rangle$ and $|\uparrow\rangle \equiv |^2S_{1/2}; F = 1, m_F = 0\rangle$, separated by 12.6 GHz. Fluorescence detection of the "bright" $|\uparrow\rangle$ state works on the $^2S_{1/2}(F = 1) \to {}^2P_{1/2}(F = 0)$ transition [Fig. 2(a)], which is closed to the $F = 0$ $|\downarrow\rangle$ state except via weak off-resonant leakage. The UV hyperfine repump [Fig. 2(a)] is not active during qubit detection so the "dark" $|\downarrow\rangle$ state is far off resonant and does not fluoresce, thus providing the state selectivity necessary to distinguish the qubit states. To within off-resonant couplings, the 935.2-nm repump maintains the state selectivity of the fluorescence during detection since it uses the $^2D_{3/2}(F = 1) - {}^3D[3/2]_{1/2}(F = 0)$ transition that is, again, nominally closed to the $|\downarrow\rangle$ state by angular-momentum selection rules.

The qubit detection is not a steady-state fluorescence problem like that considered in the previous sections. Off-resonant leakage between states introduces a time dependence and gradually spoils the state selectivity during detection. There are several leakage processes to be considered in the detection cycle including those within the repump transition. Under ideal circumstances, the dominant process during detection of the bright $|\uparrow\rangle$ state is off-resonant UV pumping into the dark $|\downarrow\rangle$ state via the excited $^2P_{1/2}(F = 1)$ level and a resulting cessation of fluorescence. The dominant leakage process for the $|\downarrow\rangle$ state is off-resonant pumping into the bright-state fluorescence cycle via the same excited state. The leakage rate during detection of the $|\uparrow\rangle$ state is derived as follows, assuming the laser is far detuned from the leakage transition, and the polarization is optimal linear with $\theta_{BE} = \theta_0$:

$$\gamma_{L,b} \approx \frac{2}{27}\gamma\left(\frac{\Omega}{2\Delta_{p,\mathrm{HF}}}\right)^2 \mathcal{P}_{s1}^{(r)}, \tag{11}$$

where $\mathcal{P}_{s1}^{(r)}$ is the total steady-state population in the ground-state $^2S_{1/2}(F = 1)$ manifold during fluorescence assuming no leakage. For typical magnetic fields considered in this experiment, the repump correction associated with the low-lying $^2D_{3/2}$ state is small and the ground-state population simplifies to $\mathcal{P}_{s1}^{(r)} \approx \mathcal{P}_{s1} = 1 - \mathcal{P}_{p0}$. The value of $\mathcal{P}_{p0}$ is given by Eq. (2).

The leakage rate during detection of the $|\downarrow\rangle$ state is as follows:

$$\gamma_{L,d} \approx \frac{2}{9}\gamma\left(\frac{\Omega}{2(\Delta_{s,\mathrm{HF}} + \Delta_{p,\mathrm{HF}})}\right)^2. \tag{12}$$

Since the ground-state hyperfine splitting is substantially larger than that of the excited state ($\Delta_{s,\mathrm{HF}} \gg \Delta_{p,\mathrm{HF}}$), there is an asymmetry in the leakage rates shown in Eqs. (11) and (12) and the limitation on detection is ultimately the bright-state leakage.

Detection fidelity from fluorescence scattering relies on being able to discriminate between fluorescence counts in a single shot. Ignoring leakage processes and other imperfections, the collected photon counts during $|\uparrow\rangle$ state detection is governed by Poissonian statistics, while the $|\downarrow\rangle$ state is fully dark. A minimum of about 10 photons on average needs to be collected to separate the Poissonian distribution cleanly from zero counts for an ideal fidelity far exceeding 99%. This value is reduced by detection errors due to the leakage processes

already discussed as well as other effects such as background counts. The detection fidelity based on leakage rates can be summarized in terms of the photon collection efficiency η, the average number of collected photons $\lambda_0 = \eta\gamma\mathcal{P}_{p0}^{(r)}t_d$ during detection time t_d, and the ratios of leakage rate to scattering rate by the ion, $\alpha_{\{b,d\}} = \gamma_{L,\{b,d\}}/(\gamma\mathcal{P}_{p0}^{(r)})$. The reader is referred, for example, to Ref. [13]. Here we briefly summarize those results and extend them to account for coherent population trapping among other effects.

Using Eq. (2) and assuming $\theta_{BE} = \theta_0$ as well as an on-resonant detection laser, the leakage rates convert to α parameters as follows:

$$\alpha_b = \frac{2}{3}\left(\frac{\Gamma_{171}}{2\Delta_{p,\mathrm{HF}}}\right)^2(1-\mathcal{P}_{p0})$$
$$\alpha_d = 2\left(\frac{\Gamma_{171}}{2(\Delta_{p,\mathrm{HF}}+\Delta_{s,\mathrm{HF}})}\right)^2. \tag{13}$$

Note the repump correction does not appear in these expressions. The probability $p_b(n)$ of collecting n photons for the $|\uparrow\rangle$ state, including the leakage effect is as follows [13]:

$$p_b(n) = e^{-\alpha_b\lambda_0/\eta}\left[\frac{e^{-\lambda_0}\lambda_0^n}{n!} + \frac{\alpha_b/\eta}{(1+\alpha_b/\eta)^{n+1}} \times \frac{1}{n!}\Gamma(n+1,(1+\alpha_b/\eta)\lambda_0)\right]. \tag{14}$$

This describes a convolution of the probability to pump dark at time t with the probability of having collecting n photons from the Poissonian scattering distribution up to that time. The ion is assumed to remain dark after the pumping event. The first term in Eq. (14) is associated with no pumping error, while the second term, which accounts for a pumping error at any point in the detection period t_d, is written in terms of the incomplete Γ function $\Gamma(a,x) = \int_0^x e^{-y}y^{a-1}dy$.

For the $|\downarrow\rangle$ state the probability $p_d(n)$ of collecting n photons is as follows [13]:

$$p_d(n) = e^{-\alpha_d\lambda_0/\eta}\left[\delta_n + \frac{\alpha_d/\eta}{(1-\alpha_d/\eta)^{n+1}} \times \frac{1}{n!}\Gamma(n+1,(1-\alpha_d/\eta)\lambda_0)\right]. \tag{15}$$

The interpretation of this equation is similar to that for Eq. (14) and accounts for the probability for the $|\downarrow\rangle$ qubit state to pump bright during the detection interval. The ion is assumed to remain bright after the pumping error. Because of the asymmetry in leakage rates between the bright and dark qubit states this is not a good approximation in general but is acceptable near where the fidelity is highest.

The single-shot fidelity of detecting either the bright $|\uparrow\rangle$ state or dark $|\downarrow\rangle$ state with a discriminator level set to collected photon number n_o is

$$F_b = \sum_{n>n_o} p_b(n) \quad F_d = \sum_{n\leqslant n_o} p_d(n). \tag{16}$$

For concreteness, a photon collection efficiency of $\eta = 3\times10^{-3}$, Zeeman shift $\delta_B/2\pi = 8.2$ MHz, saturation parameter $s_0 = 1.9$, and detection time $t_d = 0.4$ ms give an average photon count for the bright $|\uparrow\rangle$ state of $\lambda_0 \approx 10$ and an expected detection error with $n_0 = 0$ of $1-F_b = 0.007$ for the $|\uparrow\rangle$ state and $1-F_d = 0.004$ for the $|\downarrow\rangle$ state. As already mentioned, the $|\uparrow\rangle$ state has the larger error because of a larger leakage rate and limits the overall qubit detection fidelity. This example provides ideal values that must be corrected for experimental effects due to background counts and actual leakage rates.

III. EXPERIMENT

The ion trap used in this experiment (Fig. 3) is a linear Paul trap composed of four 0.48-mm diameter tungsten rods held in a square configuration by ceramic spacers at either end. Center-to-center distance of the rods is 1.27 mm. Two opposing rods are rf grounded and the other two are connected to a 30-MHz radio frequency source through a quarter-wave resonator to confine the ion radially. Two tungsten needles separated by 2.30 mm are connected to approximately 26 V, confining the ion in the axial direction. Secular trap frequencies obtained are $\{\nu_{r1},\nu_{r2},\nu_{\mathrm{axial}}\} = \{0.41,0.43,0.18\}$ MHz. The rods are also independently dc biased by 0–100 mV to suppress the micromotion of the ion.

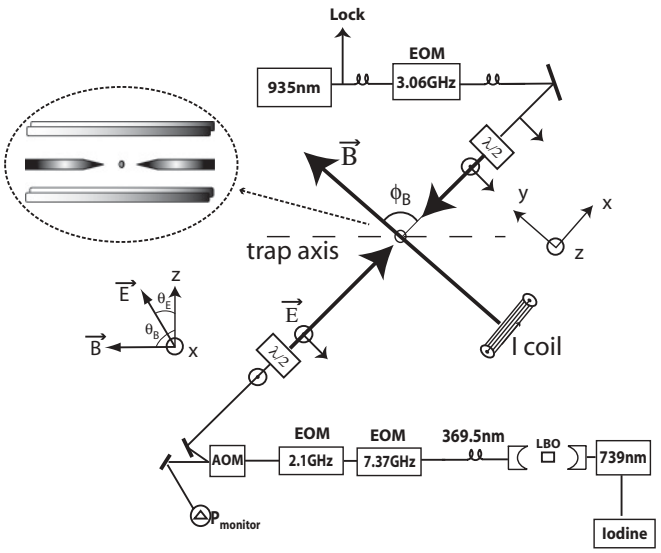

FIG. 3. Schematic of essential experimental details for Doppler laser-cooling and fluorescence detection of trapped Yb^+ ions. The primary 369.5-nm transition is driven by a frequency-doubled 739-nm diode laser system, frequency narrowed and long-term stabilized to molecular iodine. About 200 μW of the fiber-coupled UV power is directed through two free-space resonant EOMs for UV hyperfine repump at 7.37 GHz (second sideband) and hyperfine-qubit initialization at 2.105 GHz. An 80-MHz AOM directs ~60 μW to the trap while the zero order is used as a power drift monitor. Before being focused into the trap, the 369.5-nm beam has its vertical polarization rotated as shown by angle $\theta_E = 2\theta_{\lambda/2}$ as it passes through a half-wave plate oriented at $\theta_{\lambda/2}$ from the vertical. The 369.5-nm laser is focused into the trap along the axis defined to be $\hat{x}$. The 935.2-nm repump transition is driven by a stabilized diode laser which is fiber-coupled into a broadband fiber modulator for hyperfine repumping and passes through a half-wave plate before being focused into the vacuum chamber. A single magnetic coil provides a magnetic bias field with direction defined by spherical coordinates θ_B and ϕ_B. The field is nominally directed along the $\hat{y}$ axis. The inset shows the orientation of the linear Paul trap within the vacuum chamber.

The trap is kept in an ultrahigh vacuum system achieving single-ion trap lifetimes from several hours to several days. To load ions into the trap, a stainless steel tube filled with ytterbium metal is resistively heated to send evaporated Yb atoms toward the trap. The atoms are ionized in an isotopically selective and (presumed) two-color photoionization process [7]. A 398.9-nm external-cavity diode laser is used to resonantly excite neutral Yb atoms from the $^1S_0$ to the $^1P_1$ state. From there, a 369.5-nm photon from the ion laser-cooling beam has sufficient energy to remove the electron to the continuum. The 398.9-nm laser is overlapped with a relatively high-power 2-mW 369.5-nm laser beam during loading to obtain good photoionization efficiency. The 398.9-nm laser beam has a waist diameter of 60–100 μm and is maintained at a reduced power of about 300 μW to limit saturation broadening and improve isotopic selectivity.

Once trapped, ions are Doppler cooled on the $^2S_{1/2}(F = 1) -^2 P_{1/2}(F = 0)$ transition by a 369.5-nm beam produced by a frequency-doubled, amplified diode laser system at 739 nm. The laser system produces about 4-mW of UV power and 2 mW of it is fiber coupled to the experiment. The majority of the fiber-coupled beam goes to a path used during loading while about 200 μW is directed to the primary beam line used for laser cooling, optical pumping, and fluorescence detection of the ions. The primary beam line (Fig. 3) consists of two resonant electro-optic modulators (EOMs) at 2.1 and 7.37 GHz. The second sideband of the 7.37-GHz EOM is used to repump $^{171}Yb^+$ from the $^2S_{1/2}(F = 0)$ to maintain steady-state fluorescence. The first sideband of the 2.1-GHz EOM can be activated to drive the optical pumping transition $^2S_{1/2}(F = 1) - {}^2P_{1/2}(F = 1)$ to initialize the ion to the $|^2S_{1/2}; F = 0, m = 0\rangle$ state (see Fig. 2). An 80-MHz acousto-optic modulator (AOM) provides fast control of the UV laser power incident on the ion. A maximum of roughly 60 μW reaches the trap where the laser beam's waist diameter is 60 μm.

In order to keep the ion in the cooling and detection cycle, stabilized external-cavity diode lasers at 935.2 nm and 638.6 nm are used to repump the ion from the metastable $^2D_{3/2}$ and $^2F_{7/2}$ states, respectively. Roughly 2 mW of 638.6-nm laser power is overlapped with the 369.5-nm cooling beam and sent to the trap. Up to 3 mW of 935.2-nm laser power is delivered through an independent beam path (Fig. 3) and focused to a beam waist diameter of 200 μm. The 935.2-nm beam is additionally frequency modulated with a broadband fiber modulator at 3.07 GHz to provide hyperfine repumping from the $^2D_{3/2}(F = 2)$ state. The 935.2-nm beam and modulation sidebands are left continuously on during the experiment, as is the 638.6-nm laser.

Additional specific details relevant to the ion fluorescence measurements are highlighted as follows:

Laser detuning control and stability. To ensure stable detuning and narrow linewidth, the 739-nm laser is short-term stabilized using its doubling resonator cavity as a reference. Long-term drifts are suppressed by locking the laser to an iodine hyperfine feature near 739.034 nm [35] using a saturated absorption setup. The 935.2-nm laser is stabilized against slow drifts by a transfer lock setup which consists of a confocal Fabry-Perot cavity locked to the iodine-stabilized 739.05-nm laser. The 935.2-nm linewidth is also narrowed using the transfer lock signal and fast current feedback to the diode laser. A broadband fiber EOM in the lock paths for both the 739.05- and 935.2-nm lasers allows each laser to be frequency tuned while locked.

Laser power control. The 80-MHz AOM in the 369.5-nm primary beam line is used to perform automated scanning of the laser power incident on the ion. Power calibrations of the AOM response using a photodiode power meter are done to limit day-to-day systematic errors in the power dependence of the ion's fluorescence to better than 10%. The power calibration is made at the entrance to the vacuum chamber with only about 8% reduction at the ion expected due to reflection from the uncoated vacuum ports. The AOM's zeroth order is also used to monitor the UV power during data collection in order to correct for laser power drifts in subsequent analysis.

Polarization control. The polarization of the 369.5- and 935.2-nm beams are initially linearly polarized by polarizing beam splitter cubes. Zero-order quartz half-wave plates are used to adjust the polarization of each. The basic behavior of the UV half-wave plate in particular is verified off-line.

Photon collection. Scattered photons from a trapped ion are collected with an anti-reflection-coated UV microscope objective lens with high numerical aperture (NA ≈ 0.23) and the image is relayed to a intensified charge-coupled device (CCD) camera for diagnostic purposes or to a photomultiplier tube (PMT) for measurement of the ion fluorescence by photon counting. The net photon collection efficiency of the imaging system is about 3×10^{-3}. The PMT's detection efficiency is not spatially uniform. To suppress drifts in photon count rates, we check the position of the ion's image on the CCD camera consistently during the experiment and adjust the imaging system as needed. A pinhole is inserted at an intermediate image plane to suppress background scatter from the trap electrodes. A dichroic mirror is also used in the imaging optical path to suppress all except UV photons from reaching the camera and PMT. The 638.6- and 935.2-nm lasers do not appreciably contribute to the PMT background count rate.

Magnetic field. The magnetic field in the trap is generated by a single Helmholtz coil. Field homogeneity is not an issue since the trap and ion's position are essentially fixed relative to the coil. The magnetic field is arranged to be nominally along the y direction, orthogonal to the UV laser beam direction (see Fig. 3).

Microwaves. A microwave horn delivers 12.6-GHz radiation to the trapping region in order to drive transitions between arbitrary hyperfine ground states of $^{171}Yb^+$. A typical Rabi frequency of 10–20 kHz is achieved. The microwaves are used both for magnetic field calibration and state preparation of the $|^2S_{1/2}; F = 1, m_F = 0\rangle$ qubit state.

IV. RESULTS

The fluorescence behavior of $^{171}Yb^+$ is presented first since the ion is used for calibrations of magnetic field and laser polarization. Fluorescence behavior for the simple "control" ion $^{174}Yb^+$ is then presented with a comparison of the two isotopes. Finally, the fluorescence of $^{171}Yb^+$ ion is revisted in the context of state-selective detection of the hyperfine qubit.

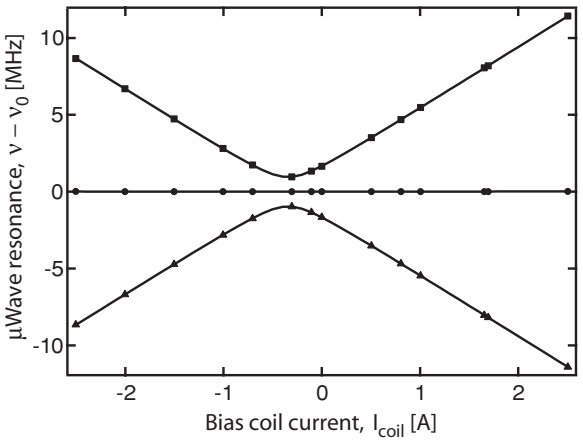

FIG. 4. Calibration of magnetic field at trapped ion's location using microwave spectroscopy of ^{171}Yb$^+$. Shown are measured transitions from ground hyperfine state $|F=0,m_F=0\rangle$ to $|F=1,m_F=-1\rangle$ (triangles), $|F=1,m_F=0\rangle$ (circles), and $|F=1,m_F=+1\rangle$ (squares) as a function of bias coil current I_{coil}. Vertical axis is referenced to inferred resonance frequency $\nu_0 = 12\,642.8$ MHz at zero magnetic field. Solid lines are a fit to Breit-Rabi theory with three magnetic-field parameters, (i) current-dependent Zeeman shift 3.991(2) MHz/A corresponding to $dB/dI = 2.851(1)$ G/A, (ii) offset current $I_o = -0.344(1)$ A, and (iii) minimum Zeeman splitting 0.952(7) MHz. The last two parameters characterize a constant background field of about 1 G. The fit lines match the data to ±10 kHz.

A. Magnetic field calibration

The magnetic field strength at the trap is calibrated *in situ* using microwave spectroscopy of the ^{171}Yb$^+$ hyperfine ground state. Resonances of all three microwave Zeeman transitions $|^2S_{1/2};F=0,m_F=0\rangle \rightarrow |^2S_{1/2};F=1,m_F=0,\pm 1\rangle$ are measured to extract the Zeeman shift between the $F=1$ sublevels as a function of magnetic bias coil current I_{coil}. The measurement cycle begins with a 2.6-ms period of Doppler cooling, followed by optical pumping for 0.3 ms to prepare the ion in the $|^2S_{1/2};F=0,m_F=0\rangle$ state. A microwave pulse close to a π pulse is applied, and state-selective fluorescence detection (discussed in detail in Sec. IV H) is used to probe the population transfer as a function of microwave frequency. The frequency is scanned to obtain a Rabi line shape, which is fit for resonance location. The measurement cycle is repeated 50 times to average detection noise. At each bias coil current, UV laser power and detection time (0.4–4 ms) are adjusted to optimize the state detection efficiency.

The Zeeman-shifted resonances obtained for all three hyperfine transitions are plotted as a function of bias coil current in Fig. 4. The magnetic field dependence of the resonances are fit to the Breit-Rabi theory together with a parametrization of both current-dependent and static-background magnetic fields. Resonance at zero magnetic field is inferred from the fit to be near 12 642.81 MHz. We extract a coil-dependent linear Zeeman shift of 3.991(2) MHz/A, corresponding to magnetic field calibration $dB/dI = 2.851(1)$ G/A. Although the fit includes the quadratic Zeeman effect, we ignore it in further analysis, which constitutes an error of only 20 kHz at the largest currents considered.

A nonzero minimum Zeeman shift of $\delta_B = 0.952(7)$ MHz occurs at a value of $I_{\text{coil}} = -0.343(1)$ A, which indicates a residual static background field of 0.98 G parallel and 0.68 G transverse to the coil. The static background field is largely stable over the course of days and longer (better than 100-kHz drift) so we simply incorporate it into our calibration. The majority of the fluorescence data is taken over coil currents in the range 0.8–2.5 A, where the coil field dominates and the magnetic field changes only slightly in direction due to background. Common values of coil current used are $\{0.805,1.695,2.505$ A$\}$ corresponding to $\delta_B/2\pi = \{4.68,8.19,11.41$ MHz$\}$.

B. ^{171}Yb$^+$: resonance

Modeling the ion's fluorescence behavior relies on a reasonably accurate calibration of laser detuning. The 935.2-nm repump laser is regularly checked to be on resonance during data taking. The location of the primary 369.5-nm UV transition for ^{171}Yb$^+$ is verified on a day-to-day basis using a Zeeman shift $\delta_B/2\pi = 8.19$ MHz, near-optimal polarization angle corresponding to $\theta_{BE} = 57.5^\circ$ and a laser power set to a relatively low saturation value. The frequency-doubled 369.5-nm laser frequency is scanned by tuning the iodine lock offset frequency of the 739-nm fundamental. The fluorescence counts, recorded in a 10-ms interval and averaged 10 times, are plotted as a function of UV laser frequency in Fig. 5. The scan starts below resonance and proceeds up to and past the resonance position. Because of the mechanical effects of the laser scattering, the trapped ion is heated on the high side of resonance and is effectively Doppler shifted off resonance. This results in a characteristic half line shape [36] where the standard procedure is to identify the drop-out as resonance. The background-subtracted data are fit to a Lorentzian line shape with an exponential suppression above

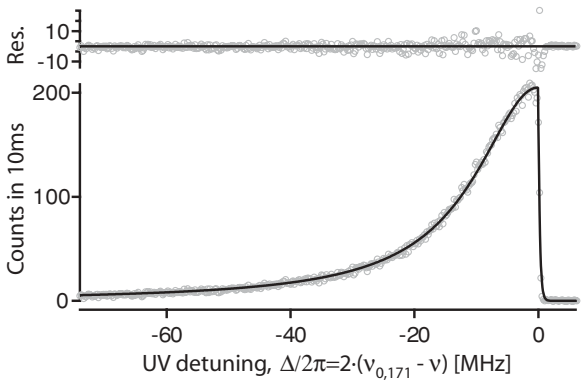

FIG. 5. Scan of UV laser frequency to locate resonance of a single trapped ^{171}Yb$^+$ ion. The frequency-doubled laser is scanned with the fundamental locked to iodine by tuning lock offset frequency ν relative to resonance $\nu_{0,171}$. Data shown are taken at $\delta_B/2\pi =$ 8.19 MHz, $s_0 = 1.590(4)$, and $\theta_{BE} = 57.5^\circ$. The line is a fit to a Lorentzian with exponential suppression above resonance. Residuals are shown in the top panel. Fit parameters are a peak amplitude coefficient, lock offset on resonance $\nu_{0,171} = 10\,193.00(5)$ MHz, and linewidth 24.6(2) MHz, where errors include sensitivity to initial guesses. The horizontal axis is recalculated using the fit value of $\nu_{0,171}$.

resonance. The fit resonance location for $^{171}Yb^+$ is at a lock offset frequency $\nu_{0,171} = 10\,193.00(5)$ MHz which includes various AOM offsets and corresponds to a fundamental laser wavelength of approximately 739.0520(1) nm as determined by a wavemeter [37]. The value of $\nu_{0,171}$ is stable to 0.1 MHz or better over several weeks.

The residuals in Fig. 5 demonstrate that there is no substantial distortion from a Lorentzian line shape. Micromotion is nulled to a level where the residual effect might only be a slight broadening. Doppler broadening is complicated by variation in the laser's cooling effect with detuning below resonance; however, at our level of precision, the overall correction to the line shape should amount to a small, if not negligible, increase in the width [36]. The fit linewidth of 24.6(2) MHz combined with calibrations of Zeeman splitting, polarization, and power saturation parameter $s_0 = 1.590(4)$ gives an inferred natural linewidth, ignoring other broadening effects, of 20.1(2) MHz. The fit linewidth is susceptible to systematics associated with the half-resonance and with points at the peak where the ion begins to decrystallize. A Lorentzian fit to data 1 MHz below resonance with the resonance location fixed gives a slightly lower linewidth 24.3(1) MHz and inferred natural linewidth 19.8(1) MHz. The dominant source of broadening is likely the laser linewidth which, if Lorentzian, would directly add to the 19.6-MHz natural linewidth. A laser linewidth of ~0.5 MHz would not be surprising. We do not correct our theory for the relatively small laser linewidth, but leave it as a systematic error. Some additional resonance and linewidth studies are presented later using the $^{174}Yb^+$ isotope.

C. $^{171}Yb^+$: polarization

The polarization dependence of $^{171}Yb^+$ fluorescence is now studied at fixed detuning and various Zeeman splittings and compared to the theory presented in Eqs. (2) and (3). The fluorescence signal strongly depends on the incident 369.5-nm laser's polarization. We take advantage of this sensitivity in our analysis to calibrate the laser polarization with respect to the magnetic field quantization direction as a function of bias coil current. The magnetic field direction changes with the current because of the presence of a residual ~1 G background magnetic field. Thus the polarization calibration's primary role is to correct for the magnetic field direction (to within directional symmetries and ambiguities).

Defining the UV laser's polarization to lie in the x-z plane (Fig. 3), the angle θ_{BE} between magnetic field, and UV polarization can be expressed in terms of angular coordinates θ_B and ϕ_B of the magnetic field and the orientation θ_E of the laser's electric field as

$$\cos\theta_{BE} = \cos\theta_E \cos\theta_B + \sin\theta_E \sin\theta_B \sin\phi_B, \qquad (17)$$

where the angle $\theta_E = 2\theta_{\lambda/2}$ is controlled by half-wave plate orientation $\theta_{\lambda/2}$ as defined in Fig. 3.

We have studied the effect of UV polarization angle on $^{171}Yb^+$ fluorescence for four different bias coil currents $\{-0.343$ A, 0.805 A, 1.695 A, 2.505 A$\}$ corresponding to Zeeman shifts $\delta_B/2\pi = \{0.95$ MHz, 4.67 MHz, 8.17 MHz, 11.39 MHz$\}$. The current -0.343 A is chosen to be close to the minimum Zeeman shift in Fig. 4. This permits an assessment of the background magnetic field orthogonal to that provided by the bias coil. The detuning of the 369.5-nm laser is chosen to be $\Delta/2\pi = -8.0$ MHz to maintain good laser cooling during data collection. In preparation for the measurements, the polarization of the 935.2-nm laser is adjusted to optimize the repump rate. The 935.2-nm laser power is also adjusted to be large enough to reduce sensitivity to beam pointing and detuning drifts, but not so large that the repump rate is significantly compromised by coherent population trapping. The UV fluorescence is not particularly sensitive to the repump parameters; therefore, the parameters are left fixed for all bias coil currents with the one exception being the value -0.343 A where the low Zeeman splitting of 0.95 MHz requires the 935.2-nm power to be reduced by a factor of roughly 10.

For each coil current, the polarization of the 369.5-nm laser is first set near to its optimal polarization angle and the laser power is scanned to identify the value where the UV fluorescence peaks [Eq. (5)]. The laser power is set to this value to reduce sensitivity to power drifts. Values used for -0.342, 0.805, 1.695, and 2.505 A are 1.4, 6.5, 10.1, and 15.6 μW, respectively. The 369.5-nm polarization is then varied by changing the half-wave plate angle. For each angle, PMT counts are recorded in three 1-s intervals and averaged to obtain the fluorescence signal.

The fluorescence data for the four coil currents are corrected for background and plotted as a function of polarization angle θ_E in Fig. 6(a). The value of the peak fluorescence varies with Zeeman shift δ_B, which is due to coherent population trapping and will be discussed in the following section. That aside, all four plots show common features: a sharp minimum corresponding to $\theta_{BE} = 90^\circ$ and a broad minimum corresponding to $\theta_{BE} = 0^\circ$ or π-polarized laser field. The sharp minima at the higher Zeeman shifts are greater than 10 times more sensitive to polarization variation compared with Malus's law. The fact that the sharp minima show good contrast indicates that the 369.5-nm laser has good linear polarization at the ion. The worst contrast occurs for the case of -0.343 A and is attributed to nonideal polarization behavior near the minimum's location. The change in location of the sharp minimum for different bias coil currents is due to change in the magnetic field direction and is primarily sensitive to variation in the coordinate θ_B.

For an arbitrary magnetic field direction, a sharp minimum will always exist that is fully dark in the ideal case since it is always possible to find a perpendicular laser polarization by rotating the half-wave plate. On the other hand, for the broad minimum, the minimum value of the fluorescence depends on how close the laser field comes to parallel polarization over the range of the half-wave plate, which in turn depends on the magnetic field orientation set by coordinate ϕ_B. Clearly for all data sets, the broad minimum is quite low so the magnetic field is always approximately in the plane of rotation of the laser polarization vector, that is, $\phi_B \approx 90^\circ$.

To fit the data we first parametrize the coil and static-background magnetic vectors in terms of magnitude constraints obtained from the magnetic field calibration and a minimum set of three angular coordinates. We then perform a weighted global fit of data from all bias coil currents to Eqs. (7) and (2). The 935.2-nm repump factor is included in the fit function and is calculated as a function of magnetic field based on separate calibration measurements. The correction to

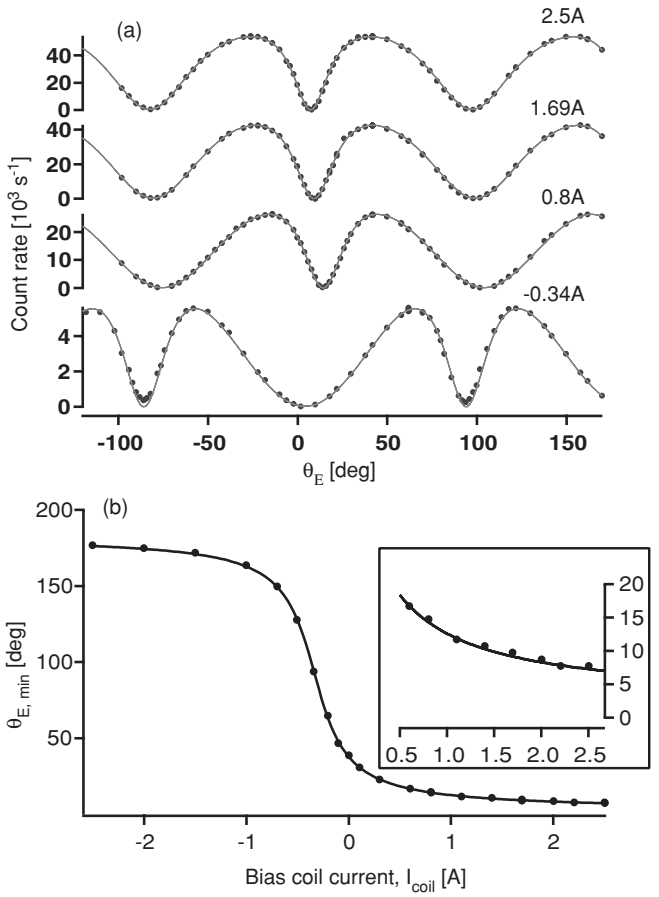

FIG. 6. (a) Fluorescence counts for $^{171}Yb^+$ versus 369.5-nm laser-polarization angle θ_E at four different magnetic bias coil currents $\{-0.343,0.805,1.695,2.505\}$, A corresponding to Zeeman shifts $\delta_B/2\pi = \{0.95,4.67,8.17,11.39\}$ MHz. Laser powers at 369.5 nm are $\{1.4, 6.5, 10.1, 15.6\}$ μW respectively. Detuning is -8.0 MHz for all data. Counts are recorded in 1-s intervals, averaged three times. Error bars, which are smaller than data markers, are the quadrature sum of Poissonian error and 0.4° uncertainty in θ_E transferred to the vertical axis through slope interpolation. Lines show a global weighted fit to all currents with four parameters to account for dependence of magnetic field orientation on coil current and residual background field, three amplitude coefficients with independent values for 0.8 A and -0.34 A plots, and a single saturation power 1.262(8) μW for all data. The fit to 206 points, which excludes select data (see text), gives a reduced χ^2 of 0.97. (b) Location $\theta_{E,\min}$ of the sharp minimum as a function of magnetic bias coil current. Inset shows a magnified scale in the range 0.8–2.5 A used in subsequent data. The line shows the prediction obtained from the global fit in (a).

the UV fluorescence rate is small, less than 2% maximum, for all magnetic fields considered.

Error bars used for the fit weighting are the quadrature sum of Poissonian error and 0.4° uncertainty in θ_E transferred to the vertical axis through slope interpolation. Nevertheless, the fluctuations in the data are completely dominated by various systematic errors. The fit is performed for a selected subset of 206 data points, about two-thirds of the total data, and gives a reduced χ^2 of 0.97 for eight fit parameters. Excluded points include several outliers, points near the sharp minima of -0.343 A data, and data at angles larger than $\theta_E = 70°$ where the half-wave plate shows a small but noticeable nonideal behavior. Regardless, it is clear from Fig. 6 that the fit is qualitatively quite good overall.

As mentioned above, the fit uses eight free fit parameters. The -8.0-MHz laser detuning and appropriate Zeeman shifts are held fixed in the fit. Besides the three angles used to parametrize the magnetic field direction, a small shift of 0.024(1) G accounts for drift in the magnitude of the background field parallel to the coil. Three amplitude coefficients of 367.7(2), 363.0(4), and 349.9(8) for the 1.7 and 2.5-, 0.8-, and -0.34-A plots respectively allow for variability in the photon collection efficiency η. Finally, the fit imposes a single saturation power 1.262(8) μW for all data. The amplitude coefficients $\mathcal{A} = 10^{-3}\eta\gamma$ in terms of kilohertz count rates convert to collection efficiency $\eta \approx 2.9 \times 10^{-3}$. For typical currents $\{0.805$ A, 1.695 A, 2.505 A$\}$ the *total* magnetic field's angular coordinates evaluated from the global fit are $\theta_B = \{104.25(3)°,99.15(4)°,97.26(4)°\}$ and $\phi_B = \{87.26(7)°,87.60(5)°,87.73(5)°\}$. The ϕ_B values are ambiguous with $\pi - \phi_B$ but both give the same result for θ_{BE}.

To confirm the calibration of magnetic field direction obtained from the global fit, we have measured the location of the sharp minimum as a function of bias-coil current. As shown in Fig. 6(b), the prediction obtained from the global fit parameters matches the data very well over a wide range of current. Furthermore, we identify the current range 0.8–2.5 A as a useful interval where the coil's magnetic field dominates the background field and the total magnetic field's direction is reasonably constant [see Fig. 6(b), inset]. This range is the focus of fluorescence studies as a function of laser power and magnetic field in the following section.

D. $^{171}Yb^+$: laser power and magnetic field dependence

With magnetic field, laser detuning, and laser polarization calibrated, it is now possible to assess the fluorescence of $^{171}Yb^+$ as a function of laser power and Zeeman shift. The magnetic bias coil's current is limited to 0.8–2.5 A or equivalent Zeeman shift of 4.5–11.9 MHz, which provides a factor of 2.5 change in Zeeman shift but, as mentioned above, this range is small enough that the magnetic field direction remains nearly constant and orthogonal to the laser beam direction. Also the lower limit on Zeeman shift avoids excessive heating and "decrystallization" of the ion in the trap over the full range of power considered for fluorescence.

The 369.5-nm laser detuning is fixed at 8.0 MHz below resonance and the laser polarization is set to $\theta_E = 41.8°$ which is near the peak of fluorescence across the range of Zeeman splitting considered [see Fig. 6(a)]. The experiment sequence involves a 2.6-ms Doppler cooling interval followed by a 10-ms fluorescence photon counting interval. All repump beams are prior optimized and are active throughout. The power of the UV laser is scanned and for each power value the fluorescence counts are averaged 10 times for a net integration time of 100 ms. The Doppler cooling interval is at fixed power and the level is adjusted to inhibit decrystallization of the trapped ion at the low end of magnetic fields considered.

The scan of UV laser power from approximately 0–70 μW is performed at 17 values of Zeeman shift from 4.6 to

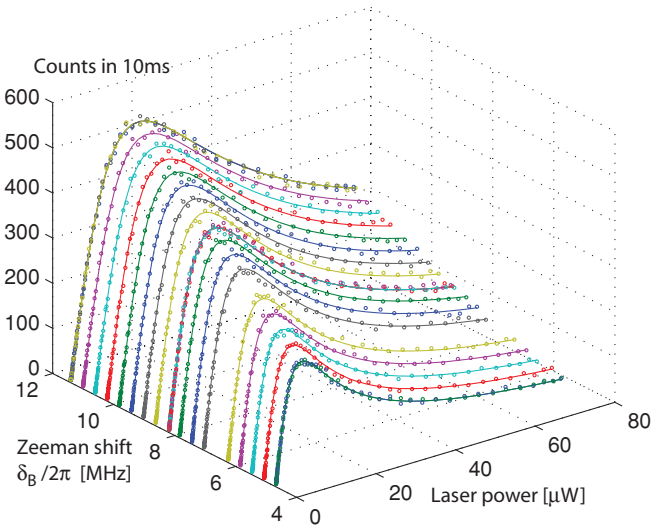

FIG. 7. (Color online) $^{171}Yb^{+}$ fluorescence versus UV laser power and Zeeman shift δ_B. The data are taken with UV detuning -8.0 MHz and laser-polarization angle $\theta_E = 41.8^{\circ}$, which is near-optimal linear polarization for all data. The lines are a single weighted global fit to all data. Error bars are suppressed for clarity. The reduced χ^2 is 1.05 for 1496 data points. Fit parameters are saturation power 1.226(1) μW, and the amplitude coefficient is 3645(2). See text and Fig. 8 for further quantitative assessment of fit.

11.4 MHz. Each scan of 68 power values takes approximately 30 s while the complete data set is acquired over 1–2 h. The counts are corrected for background and the laser power for each scan is corrected to account for slow drifts. Figure 7 shows the total data set, where the fluorescence reaches a maximum at a power value that increases with Zeeman shift δ_B. The fluorescence value at the peak also increases with increasing Zeeman shift.

Errors in the count values are determined from repeated measurements at $I_{\text{coil}} = 1.695$ A and are modeled as the quadrature sum of Poissonian and 2% fractional noise before averaging. A weighted global fit is performed with only two free fit parameters, an amplitude coefficient $\mathcal{A}$, and saturation power p_{sat}. The linewidth γ and detuning $\Delta/2\pi = -8.0$ MHz are fixed, while Zeeman splitting δ_B, polarization angle θ_{BE}, and 935.2-nm repump correction are determined as a function of bias coil current from prior calibrations. The reduced χ^2 is an acceptable value of 1.05 for 1496 degrees of freedom (8% significance). The values for the fit parameters are $p_{\text{sat}} = 1.226(1)$ μW and amplitude coefficient $\mathcal{A} = 10^{-2}\eta\gamma = 3645(2)$, giving a photon collection efficiency $\eta = 2.9 \times 10^{-3}$.

Figure 7 provides an overall impression of the quality of the global fit. Figure 8 shows quantitative detail, including data slices and global fit residuals at three example Zeeman shifts. The residuals exhibit some instabilities and discrete outliers which exceed Poissonian statistics. Nevertheless, *separate* fits of individual laser scans are often moderately acceptable with Poissonian error bars alone (reduced χ^2 below 1.3 for 66 degrees of freedom). The global fits are more challenging due to scan-to-scan drifts particularly of the amplitude coefficient (from the ion drifting relative to PMT sensitive position) but agreement is quite good overall with residuals only 2–4% near

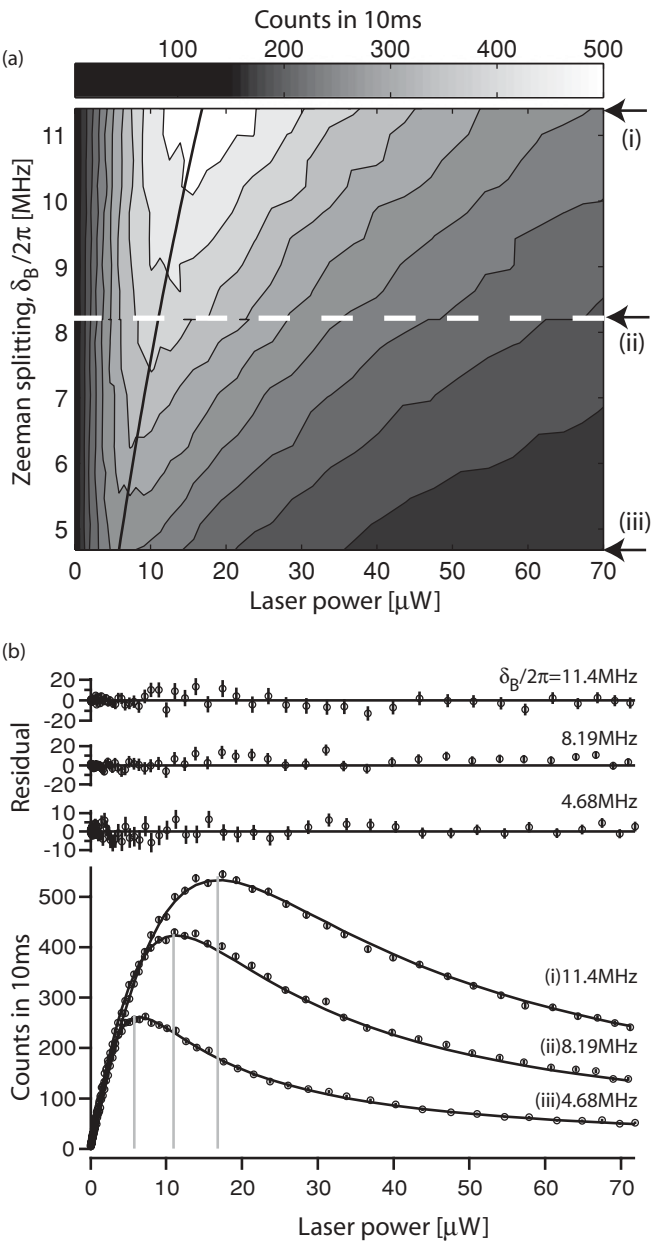

FIG. 8. (a) Contour plot of $^{171}Yb^{+}$ fluorescence counts as a function of power and magnetic field (same data set as Fig. 7). Contour scale is shown at top. The solid line is the approximate expression for power at peak fluorescence [Eq. (5)]. Arrows and horizontal dotted line indicate location of cross sections shown in (b) at three different Zeeman splittings. (b) Counts in 10 ms as a function of laser power at three Zeeman splittings $\delta_B/2\pi = \{11.41, 8.19, 4.68\}$ MHz corresponding to coil currents $\{2.50, 1.69, 0.80\}$ A. Errors, determined from repeated measurements, are the quadrature sum of Poissonian and 2% fractional error before averaging. Lines are a single weighted global fit as shown in Fig. 7. Residuals shown for each Zeeman splitting. Drop lines indicate expected peak count rate and location according to Eqs. (5) and (6) and the values of the global fit parameters.

the peak of fluorescence. Systematic errors due to detuning and linewidth have been explored qualitatively, and reasonable fits can still be obtained for small variations around the values used but with modified fit parameters.

On the contour plot of Fig. 8(a), the approximate theoretical expression for Ω_{pk} [Eq. (5)] is seen to match well with the peak location across the magnetic field range considered. In Fig. 8(b), the approximate theoretical expression for the value of the peak fluorescence $\max(\mathcal{P}_{p0})$ [Eq. (6)] is also seen to match well with the data.

As a final comment, an additional technical issue arises when scanning the power of the 369.5-nm laser. Since the 369.5-nm hyperfine repump is obtained from a modulation sideband of the 369.5-nm laser, the repump power also varies as the laser power is scanned. We have separately verified that the repump sideband power can be reduced by more than a factor of 2 without observable effect on the fluorescence curves.

E. $^{174}Yb^+$: resonance, linewidth

We now consider fluorescence for a single trapped $^{174}Yb^+$ ion as function of the same set of parameters for $^{171}Yb^+$, namely laser detuning, polarization, and power as well as magnetic field. The calibrations for magnetic field and polarization angle versus bias-coil current carry over directly to the new analysis. In the spirit of using $^{174}Yb^+$ behavior as a control to compare against $^{171}Yb^+$, we have considered some additional experiments to assess systematics, in particular resonance and linewidth determination as is discussed now.

A laser frequency scan to locate the resonance of a single trapped $^{174}Yb^+$ ion is shown in Fig. 9(a), performed in the same way as described earlier for $^{171}Yb^+$. Scan parameters include a Zeeman shift $\delta_B/2\pi = 8.19$ MHz, laser-polarization angle $\theta_E = 97.8^\circ$ corresponding to $\theta_{BE} = 2.8^\circ$, and a relatively low UV laser power of 0.83 μW($s_0 = 0.63$). As before, the frequency-doubled 369.5-nm laser is scanned with the fundamental locked to iodine by tuning the lock offset frequency. The data is fit to a Lorentzian line shape with exponential suppression above resonance. The fit gives a lock offset frequency on resonance of $\nu_{0,174} = 8975.8(1)$ MHz, which corresponds to a fundamental wavelength of approximately 739.0499(1) nm as determined by a wavemeter [37]. We lock to the identical iodine feature as for $^{171}Yb^+$. Besides resonance location, the fit provides a linewidth of 24.6(1) MHz. Combined with calibrations of magnetic field, laser polarization, and power saturation value, the fit linewidth gives an inferred natural linewidth of 20.0(1) MHz. This value, which is within 2% of 19.6 MHz, is sensitive to errors in laser power determination and ignores technical broadening such as that due to laser linewidth.

To verify that there is nothing pathological in the half-resonance curve, we have performed a control experiment where a simultaneously trapped $^{172}Yb^+$ ion is used to sympathetically cool the $^{174}Yb^+$ ion [38] while its resonance is scanned. The cooling allows the full resonance shape to be obtained [38,39]. A separate UV laser system is used to provide Doppler cooling of the $^{172}Yb^+$ isotope, whose resonance is 1.2 GHz blue detuned from $^{174}Yb^+$. The additional $^2D_{3/2}$-$^3D[3/2]_{1/2}$ repump frequency for $^{172}Yb^+$ is easily obtained by adding a modulation sideband of 2.56 GHz to the 935.2-nm laser using the preexisting fiber modulator. The 638.6-nm laser is continuously scanned at a slow rate to ensure it covers both isotopic resonances. The majority of fluorescence from the $^{172}Yb^+$ ion is blocked from reaching the PMT at an intermediate image plane in the imaging system and the remainder is subtracted as a background from the $^{174}Yb^+$ fluorescence signal of interest.

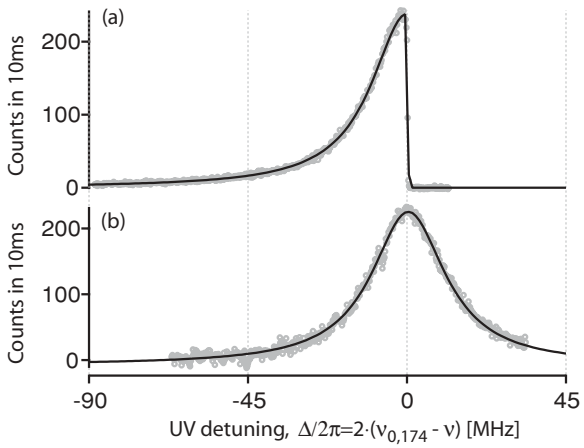

FIG. 9. (a) Scan of UV laser frequency to locate resonance of single trapped $^{174}Yb^+$ ion. The frequency-doubled laser is scanned with the fundamental locked to iodine by tuning lock offset-frequency ν. The parameters for the scan are $\delta_B/2\pi = 8.19$ MHz, $\theta_{BE} = 2.8^\circ$, and saturation parameter $s_0 = 0.63$. The solid line is a fit to a Lorentzian with exponential suppression above resonance. The fit yields a resonance location $\nu_{0,174} = 8975.8(1)$ MHz and a linewidth of 24.6(1) MHz, including all broadening terms. The horizontal axis is offset and scaled using the fit value of $\nu_{0,174}$ to indicate UV detuning. (b) Scan of UV laser frequency to locate resonance of $^{174}Yb^+$ in the presence of sympathetic cooling by simultaneously trapped $^{172}Yb^+$ ion. The horizontal scale for the scan has been shifted by 2 MHz to account for a measured ac Stark shift from the $^{172}Yb^+$ cooling laser. Other parameters are similar to (a). Fit resonance position is slightly shifted by 0.39(5) MHz relative to resonance in (a), attributed to systematic error in ac Stark shift determination. The fit linewidth is 25.5(2) MHz. The fit includes a baseline −7.6(6) to account for drifts in background $^{172}Yb^+$ fluorescence.

The resonance scan of $^{174}Yb^+$ in the presence of sympathetic cooling is shown in Fig. 9(b). The data have been corrected for residual background. Additionally, an offset of +2 MHz has been applied to the horizontal frequency scale to account for the ac Stark shift due to the $^{172}Yb^+$ cooling beam. The value of the ac Stark correction was estimated in a separate measurement. The data have been fit to a Lorentzian line shape which gives a UV resonance frequency slightly shifted by 0.39(5) MHz relative to that of the single ion shown in Fig. 9(a). The resonance shift is within the bounds of the systematic error of the ac Stark shift estimation. In any case it is at least clear that there is nothing grossly wrong with our determination of resonance using the drop-out point of a single trapped ion. The Lorentzian fit also gives a linewidth of 25.5(2) MHz, and an inferred natural linewidth of 20.9(2) MHz.

As noted previously, we do not correct the fluorescence theory for any extra broadening effects outside of the theoretical expressions presented in Eqs. (3) and (10). The largest correction is probably due to the laser linewidth. The absorption linewidths from all the resonance scans presented so far have given inferred natural linewidths within 5% of the previously published value of 19.6 MHz [25];

however, the scans are done at fixed magnetic field and laser power and require correction for Zeeman and saturation broadening to reveal any remaining effects. We have done a more careful experiment to remove the saturation broadening and constrain the size of any systematic effects such as laser linewidth. We follow a similar procedure to that used to assess magnetic field dependence of $^{171}Yb^+$ and perform relatively fast scans of laser power at several values of detuning to extract the resonance profile for the fluorescence. The laser power for each scan is scaled to correct for slow drifts. The laser sidebands required for hyperfine repump of $^{171}Yb^+$ are also kept active. They are far off resonant and have no appreciable effect but, by having them active for $^{174}Yb^+$ studies also, we are able to compare saturation powers directly between the two isotopes without correction. The data are collected at a fixed magnetic field corresponding to $\delta_B/2\pi = 8.19$ MHz and at a polarization angle corresponding to $\theta_{BE} = 2.8^\circ$.

Laser power scans of $^{174}Yb^+$ fluorescence, corrected for background, are shown in Fig. 10(a) for a selection of laser detunings. The fluorescence counts are acquired for 10 ms and averaged 10 times. The analysis makes use of the fact that $^{174}Yb^+$ data should fit to a general saturation form with repump correction. Each laser power scan at a given detuning is fit to the following equation which includes the 935.2 nm repump factor ξ explicitly:

$$\eta\gamma\mathcal{P}_p = \mathcal{A}\left[\frac{s}{1+(1+\xi/2)s}\right]. \tag{18}$$

The free fit parameters are an amplitude coefficient $\mathcal{A}$ and a proportionality constant ds/dp linking the laser power p to the generalized saturation parameter $s = (ds/dp)p$. The repump factor, estimated from separate measurements, is fixed at a value of 0.1. The general form of the equation should still apply for finite laser linewidth with modification to the linewidth and saturation power [40]. Errors used for fit weighting, determined from repeated measurements, are Poissonian with an additional 2% fractional noise before averaging. Reduced χ^2 for the fits are generally good, on average 1.0(2) for 66 degrees of freedom, except for the two detuning values nearest resonance where the trapped ion becomes motionally unstable at high laser powers. The fit amplitude coefficients are roughly constant over the range of detunings shown. At larger detunings fitting difficulties and correlations of the fit parameters become significant.

The saturation factors ds/dp obtained from the individual fits are plotted as a function of detuning in Fig. 10(b). An unweighted fit to the data is made using the following Lorentzian form obtained from Eq. (10),

$$\frac{ds}{dp} = \frac{1}{3}\frac{1}{p_{\rm sat}}\frac{\gamma^2}{[\Gamma_{174}(\Omega=0)]^2+4\Delta^2}, \tag{19}$$

where $p_{\rm sat}$ is a saturation power and the linewidth $\Gamma_{174}(\Omega = 0)$ only includes the Zeeman broadening. Although Eq. (10) and by extension Eq. (19) are derived as an approximation in general at finite magnetic field, the functional form is correct for the special case of π polarization ($\theta_{BE} \approx 0^\circ$) considered here. The fit uses only two free parameters, $p_{\rm sat}$ and the natural linewidth γ. Resonance location, determined as shown in Fig. 9, is held fixed. Excluding the two data points closest to resonance that show excess noise in fluorescence scans, the fit provides parameters $p_{\rm sat} = 1.25(1)$ μW and $\gamma/2\pi = 19.6(1)$ MHz. If the points at the peak are included, these values change to 1.28(1) μW and 20.1(2) MHz respectively. The values of the inferred natural linewidth match reasonably well with the previously published value of 19.6 MHz [25] to about the 5% level. Given this level, we simply use the previously published value in our analysis and leave any additional broadening effect as a potential systematic error in our results.

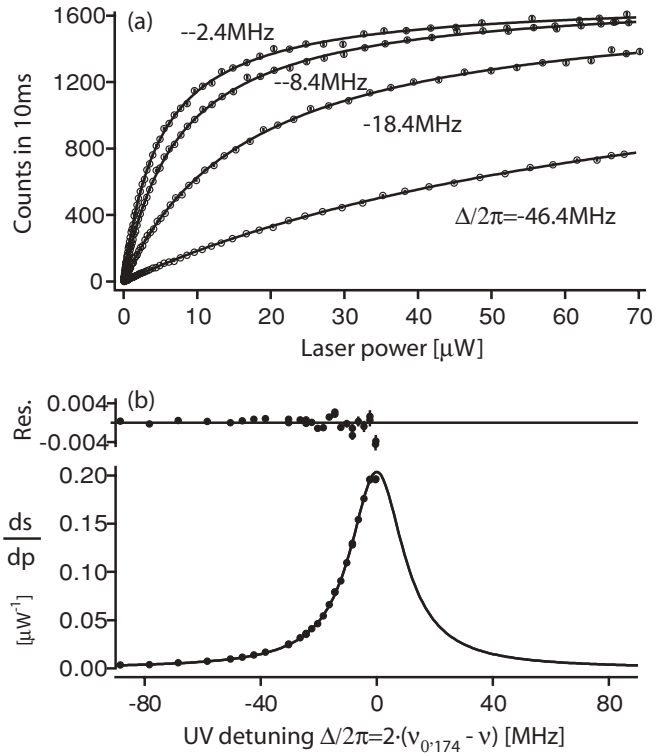

FIG. 10. $^{174}Yb^+$ resonance extracted from laser power scans at $\delta_B/2\pi = 8.19$ MHz and $\theta_{BE} = 2.8^\circ$. (a) Counts in 10 ms, averaged 10 times, are shown as a function of 369.5-nm laser power at the range of detunings indicated. Detunings are determined from resonance location as shown in Fig. 9. Errors, determined from repeated measurements, are the quadrature sum of Poissonian and 2% fractional error before averaging. Each line is a separate weighted fit to a scan at a given detuning. Fit function is a general saturation form (see text) with two fit parameters, amplitude coefficient and saturation-related factor ds/dp. Reduced χ^2 for various fits is generally good, on average 1.0(2), except for two points near resonance. (b) Plot of fit values ds/dp obtained as a function of laser detuning. The line is an unweighted fit to Eq. (10) with fixed zero baseline and fixed resonance position. Two points near the peak are excluded (see text). Residuals shown above main plot. The natural linewidth from the fit is $\gamma/2\pi = 19.6(1)$ MHz and saturation power is $p_{\rm sat} = 1.25(1)$ μW. If two points at peak are included, these values change to 20.1(2) MHz and 1.28(1) μW, respectively.

F. $^{174}Yb^+$: polarization dependence

The linewidth measurements of the previous section verified the basic frequency and saturation dependence of the resonant response of the $^{174}Yb^+$ ion at a specific magnetic

field and polarization angle. A complete comparison with $^{171}Yb^+$ requires parallel studies of the $^{174}Yb^+$ fluorescence behavior over a range of magnetic field and polarization values. As well, for a confident comparison, the approximate expression derived for $^{174}Yb^+$ fluorescence in Eqs. (9) and (10) should properly be verified. The linewidth measurements of the previous section in fact rely on Eq. (10).

The dependence of fluorescence on Zeeman splitting is very weak so we initially focus in detail on polarization dependence. The approach used for measurements differs from that for $^{171}Yb^+$. The primary behavior expected from Eq. (9) is a washing out of the polarization dependence at higher laser powers due to saturation; therefore, we focus on measuring the polarization behavior as function of laser power rather than magnetic field. The data is susceptible to drifts in laser power. To suppress their effect, we follow a similar procedure to the linewidth analysis and record relatively rapid scans of laser power as a function of laser-polarization angle θ_E and correct for slow drifts in laser power between scans.

The complete data set after background and power-drift correction is shown in Fig. 11. The magnetic bias coil current is fixed at 2.505 A to provide a Zeeman shift of 11.41 MHz. The laser detuning is set to 8.4 MHz below resonance. The variation in fluorescence is very mild in comparison with $^{171}Yb^+$ since there are no polarization dark states. Errors, as before, are assumed to be the quadrature sum of Poissonian and 2% fractional noise before averaging. A global weighted

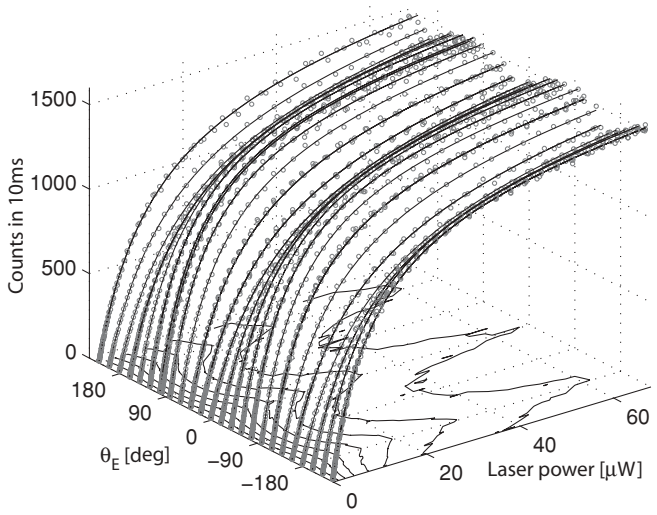

FIG. 11. $^{174}Yb^+$ fluorescence as a function of 369.5-nm laser power and linear polarization angle θ_E. Zeeman shift is $\delta_B/2\pi = 11.4$ MHz ($I_{\text{coil}} = 2.5$ A). Laser detuning is fixed at $\Delta/2\pi = -8.4$ MHz. Data consist of fifty-four 68-point scans of laser power at half-wave plate positions over a 240° range. Fluorescence photons are counted by a PMT in a 10-ms integration time, averaged 10 times. Error bars suppressed for clarity. The lines are a global weighted fit to theory in Eq. (9) with two free parameters, an amplitude coefficient 3660(2) related to photon collection efficiency, and saturation power $p_{\text{sat}} = 1.247(2)$ μW. Other parameters are fixed, including magnetic field angles as per calibration in Fig. 6. The reduced χ^2 of 1.39 for 3672 total points, while not acceptable at a reasonable confidence level, is sufficiently low to give reasonable parameter errors. See text and Fig. 12 for detailed quantitative assessment of this data and fit.

fit to the repump-corrected $^{174}Yb^+$ theory [Eqs. (7) and (9)] has been made with only two fit parameters, saturation power 1.247(2) μW and amplitude coefficient 3660(2). Other parameters in the fit are fixed, including the magnetic field coordinates $\{\theta_B, \phi_B\}$ and repump factor $\xi = 0.1$. The reduced χ^2 of 1.39 for 3672 total points, while quite poor, is sufficiently low to give reasonable parameter errors on par with an unweighted fit. The large χ^2 is attributed to systematic error associated with the approximations made in Eq. (9) and excess instabilities and scan-to-scan drifts over the several hours of data collection. Regardless, Fig. 11 shows that the fit is qualitatively good overall.

Figure 12 shows cross sections of the polarization data at three different laser powers together with the global fit prediction. Each cross section has been scaled with respect to its peak value to emphasize how the polarization dependence saturates out at high laser powers as expected. Unlike $^{171}Yb^+$, the fluorescence peaks at $\theta_E = 97.2°$, equivalent to $\theta_{BE} = 0°$, where the effective linewidth [Eq. (10)] reaches a minimum.

To emphasize the analogy with an effective two-level system, we also demonstrate the polarization analysis in an alternative way, using the same approach as for laser detuning dependence. The laser power scan at each polarization angle in Fig. 11 has been fit to the generalized saturation function [Eq. (18)] to extract the saturation derivative ds/dp as a function of θ_E. The fit values are plotted in Fig. 12(c). An unweighted fit to Eq. (19) with a single fit parameter $p_{\text{sat}} = 1.247(3)$ μW matches the data well, giving reasonably random residuals. The value for p_{sat} matches the global fit as it should.

G. $^{174}Yb^+$: Laser power and magnetic field dependence and comparison with $^{171}Yb^+$

To complete the comparison of fluorescence behavior of the two isotopes, we consider power saturation curves for $^{174}Yb^+$ as a function of magnetic field strength. Figure 13 shows fluorescence versus power for three different Zeeman shifts {4.68 MHz, 8.19 MHz, 11.41 MHz} corresponding to bias coil currents {2.505 A, 1.695 A, 0.805 A}. These three values cover the same range that we have considered for $^{171}Yb^+$. The laser polarization is set to $\theta_E = 97.8°$, which is near to the optimum value $\theta_{BE} = 0°$ relative to magnetic field for all cases within the small residual variation in magnetic field direction. The laser detuning is fixed at $\Delta/2\pi = -8.4$ MHz, which is approximately equal to that used for the $^{171}Yb^+$ power scans. The data collection sequence is the same as previous, using a 10-ms fluorescence counting time, repeated and averaged 10 times.

The fluorescence power scans, following power drift and background count correction as usual, are displayed in Fig. 13 for all three Zeeman shifts. There is only a small difference between the data since the Zeeman dependence is rather weak. A weighted global fit to the repump-corrected $^{174}Yb^+$ theory [Eqs. (9) and (7)] is applied to a set of five power scans including the three curves shown in Fig. 13. A constant repump factor of $\xi = 0.1$ is used for all magnetic field values. As before, the error model used for weighting is the quadrature sum of Poissonian and 2% fractional noise before averaging.

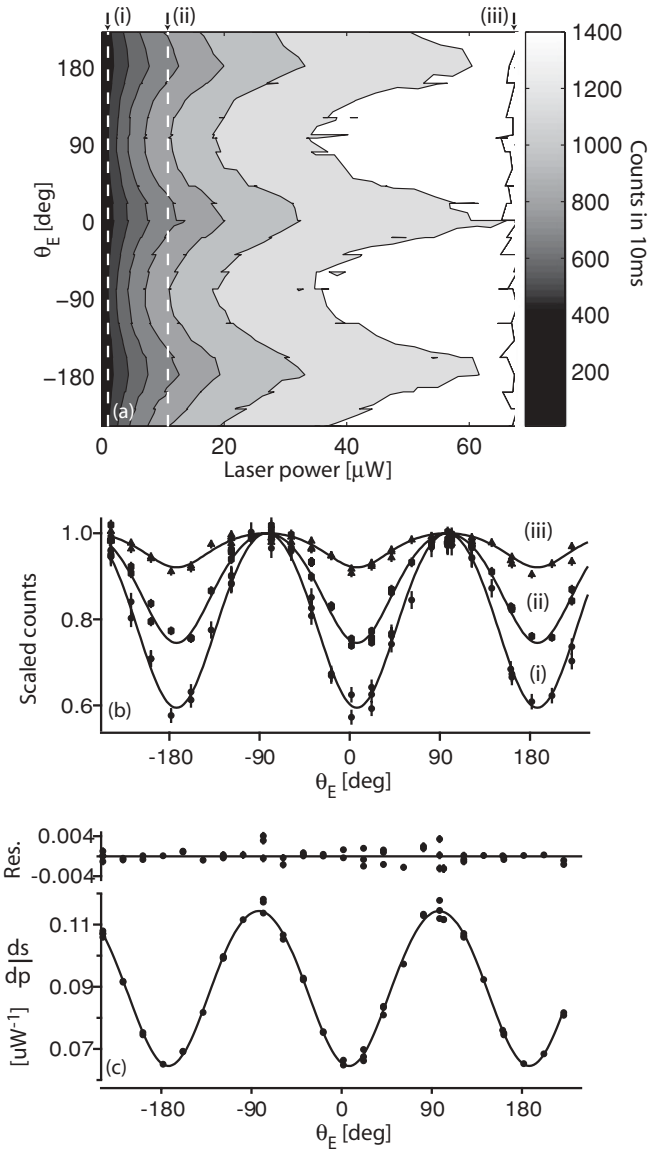

FIG. 12. (a) Contour plot of $^{174}Yb^{+}$ polarization data from Fig. 11. Lines and arrows indicate location of data cross sections in (b) at three laser powers (i) 1.1 μW, (ii) 10.5 μW, and (iii) 66.6 μW corresponding to saturation parameter s_0 of 0.9, 8.4, and 53.4 respectively. (b) Cross sections of fluorescence-count data as a function of laser-polarization angle θ_E at three laser powers mentioned above. The count rates are nomarlized to the maximum value of the fit model, occuring at $\theta_E = 97.2^\circ$, corresponding to $\theta_{BE} = 0^\circ$. Solid lines are global fits from Fig. 11. (c) Alternative polarization analysis technique using separate weighted fits of each laser power scan in Fig. 11 to a generalized saturation form to extract amplitude coefficient and saturation-related parameter ds/dp. Fit values of ds/dp are plotted as a function of polarization angle θ_E. Error bars are the statistical errors from the fits. Solid line is an unweighted fit to $^{174}Yb^{+}$ theory in Eq. (9) with one free parameter $p_{sat} = 1.247(3)$ μW. Fit residuals, showing reasonably random scatter, are included above the main plot.

Residuals for the fit are shown in the top panel of Fig. 13 since the differences between curves are slight. An acceptable reduced χ^2 of 1.07 is obtained for this relatively small data

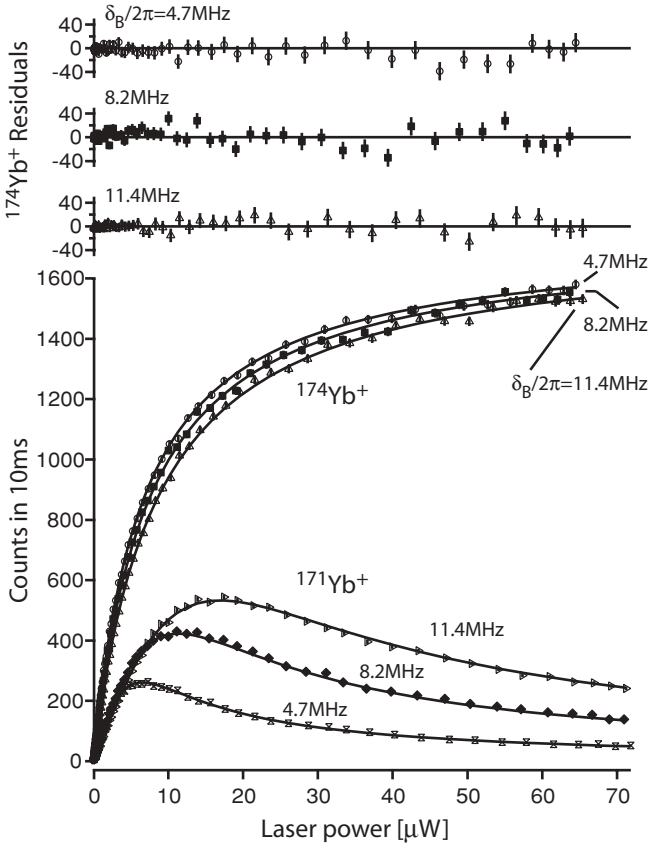

FIG. 13. $^{174}Yb^{+}$ fluorescence versus UV laser power at three magnetic fields, and comparison to $^{171}Yb^{+}$ behavior. Fluorescence counts are collected in 10-ms intervals, averaged 10 times. The three Zeeman shifts $\delta_B/2\pi = \{4.68, 8.19, 11.41\}$ MHz as indicated correspond to bias coil currents {0.80,1.69,2.50} A. The three $^{174}Yb^{+}$ scans are taken at near-optimal linear polarization $\theta_E = 97.8^\circ (\theta_{BE} = 2.8^\circ)$ and with laser detuning -8.4 MHz. The three $^{171}Yb^{+}$ scans, reproduced from Fig. 8, are taken at near-optimal linear polarization $\theta_E = 41.8^\circ (\theta_{BE} = 57.5^\circ)$ and at UV detuning of -8.0 MHz. Solid lines for $^{171}Yb^{+}$ are global fits also reproduced from Fig. 8. Solid lines for $^{174}Yb^{+}$ are a global fit to a total of five power scans (340 points) at the three magnetic field values. The fit gives a reduced χ^2 of 1.07. The two fit parameters are amplitude coefficient 3638(5) and saturation power $p_{sat} = 1.264(4)$ μW. Fit residuals for $^{174}Yb^{+}$ are shown in the top panels.

set of 304 points and two fit parameters; however, the quality of fits to larger data sets is not as good, compromised by slow drifts of the photon collection efficiency and other effects. The amplitude coefficient from the fit is $\mathcal{A} = 3638(5)$, and the fit saturation power is $p_{sat} = 1.264(4)$ μW. These values are similar to those obtained from other $^{174}Yb^{+}$ data sets shown earlier.

For direct comparison, the $^{171}Yb^{+}$ data from Fig. 8(b) for the same magnetic field and detuning conditions is reproduced in Fig. 13 and shows the overall reduction in fluorescence due to coherent population trapping. To be specific, the maximum scattering rate in Fig. 13 reached by $^{174}Yb^{+}$ at $\delta_B/2\pi = 8.19$ MHz corresponds to an excited state fraction of about $\mathcal{P}_p = 0.45$ or about 90% of the maximum 0.5. By contrast, at the same magnetic field value, the inferred excited state fraction of $^{171}Yb^{+}$ is about 0.15 at its highest point. This

is 60% of the absolute maximum 0.25 for $^{171}Yb^+$ and about 0.3 lower than the value for $^{174}Yb^+$.

A comparison of the three curves for $^{174}Yb^+$ alone shows that the fluorescence lags slightly with increasing magnetic field as the effective linewidth is Zeeman broadened and the saturation power increased. All curves, however, approach the same saturated response at high laser powers. The same lag effect is also observable for $^{171}Yb^+$ at low powers but the dominant effect is the increase in peak fluorescence with increasing magnetic field as optical pumping to the coherent dark state is countered.

Figure 13 also shows that the low power response of $^{171}Yb^+$ is significantly slower (by a factor of ~3) than that of $^{174}Yb^+$. This is not a coherent population trapping effect but rather is due to the fact that the laser power for $^{171}Yb^+$ must be split over three polarizations ($\theta_{BE} = 54.7^\circ$) to couple to all ground Zeeman states. On the other hand, π polarization alone ($\theta_{BE} = 0^\circ$) suffices in general to provide maximum fluorescence for $^{174}Yb^+$.

The amplitude coefficients obtained from the $^{174}Yb^+$ fit in Fig. 13 [$\mathcal{A} = 3638(5)$] and from the $^{171}Yb^+$ fit in Figs. 7–8 [$\mathcal{A} = 3645(2)$], are close as expected given that the value is essentially a measurement of the photon collection efficiency of the imaging system. In fact, all the fits shown previously yield close values for $\mathcal{A}$, and give a collection efficiency of about $\eta = 2.9 \times 10^{-3}$. Moreover, the saturation powers obtained from the $^{174}Yb^+$ fit [1.264(4) μW] and from the $^{171}Yb^+$ fit [1.226(1) μW] are within 5%. There may be a slight high bias for $^{174}Yb^+$ over all the data sets taken but the small level of disagreement is within the uncertainty of our day-to-day calibration of laser power and is comparable to variations in saturation power seen for a single isotope. Inclusion of the 935.2-nm repump effect was helpful to improve the agreement between isotopes since the effect acts asymmetrically. It reduces the saturation power and increases the amplitude coefficient for $^{174}Yb^+$ by about 5% but has little effect on $^{171}Yb^+$.

For a typical value of $p_{\text{sat}} = 1.26\ \mu$W and a measured beam waist diameter of 60 μm for the 369.5-nm laser, the saturation intensity is calculated to be 60 mW/cm^2. This value includes a correction of 28% to account for power lost to hyperfine repump sidebands and a correction of 8% to account for power lost from reflection at the uncoated entrance windows to the vacuum system. The value for saturation intensity matches quite well with the expected value of $I_{\text{sat}} = 51$ mW/cm^2 using the value of $\gamma/2\pi = 19.6$ MHz. As noted in Sec. II, the values calculated here are defined for a two-level cycling transition and specifically exclude factors related to the multilevel transition.

Figure 13 summarizes the fluorescence results to this point. The saturated count rate of $^{174}Yb^+$ essentially provides a simple, direct measure of the imaging system's photon collection efficiency with minimal theoretical input and largely independent of laser parameters. The simple saturation form of the fluorescence also provides a basic calibration of the saturation intensity at the ion. These two experimental numbers together with the magnetic field and polarization calibration obtained from $^{171}Yb^+$ behavior are all the experimental inputs required to calculate the expected fluorescence count rate during detection of the hyperfine qubit in $^{171}Yb^+$ ion. State-selective qubit detection is discussed in the next section as a direct application of the fluorescence studies.

H. $^{171}Yb^+$: qubit detection fidelity

To characterize the detection fidelity for the $^{171}Yb^+$ hyperfine qubit, we consider a typical Zeeman shift of 8.19 MHz (bias coil current of 1.69 A). The experiment sequence is similar to that described in the magnetic field calibration section. A 2.6-ms Doppler cooling pulse is followed by 0.3 ms of optical pumping that initializes the ion in the $|F = 0, m_F = 0\rangle$ ground hyperfine state, identified for brevity as the $|\downarrow\rangle$ qubit state. Subsequently, an optional resonant microwave π pulse can be used to transfer the ion to the $|F = 1, m_F = 0\rangle$ state, defined as the $|\uparrow\rangle$ state. The optical pumping is assumed to be near-ideal while the fidelity of the microwave transfer is estimated to be 0.994 or better, limited by timing and microwave detuning. Finally, photons are collected in a detection interval of duration t_d. The 369.5-nm detection laser is set to near-optimal polarization corresponding to $\theta_{BE} = 57.4^\circ$ and set to a detuning $\Delta/2\pi = -4.1$ MHz close to resonance. During the detection pulse, the UV hyperfine repump is deactivated to allow for differential fluorescence of the qubit states. The 935.2- and 638.6-nm repump beams are active through the experiment, including the detection period.

As discussed in Sec. II C, the qubit detection fidelity is ultimately limited by off-resonant leakage processes, which depend in particular on the 369.5-nm laser power used for detection. To assess detection errors due to leakage rates [Eqs. (11) and (12)] as well as other, technical effects, we have studied the detection as a function of the 369.5-nm laser power. For each power value, four hundred repetitions of the experiment sequence are performed to accumulate statistics of photon counts. Example histograms at two detection laser powers and for both initially prepared states are shown in Fig. 14. The detection time is $t_d = 0.4$ ms. In Fig. 14(a), which corresponds to near-optimal laser power, the $|\uparrow\rangle$ or "bright" qubit state gives an approximately Poissonian distribution of photon counts; however, at low count values, deviations from the Poissonian form are apparent that correspond to situations where the ion pumps into the $|\downarrow\rangle$ state and ceases to fluoresce. The distribution becomes increasingly distorted at higher detection laser power [Fig. 14(c)]. Detection of the $|\downarrow\rangle$ or "dark" qubit state [Figs. 14(b) and 14(d)] is dominated by zero-count events but there are events that show up in the first or so bins due to background counts from ambient light and UV laser scatter off the trap electrodes. There is also some probability for the ion to leak off-resonantly into the bright state and begin to scatter photons. This leads to a characteristic low pedestal at larger counts but the effect is too faint to be seen in the example plots. In fact, the plots show that the overall qubit detection error is dominated by background counts in $|\downarrow\rangle$ detection and leakage events in $|\uparrow\rangle$ detection.

In state-selective detection, a discriminator n_o is used to convert the distributions of photon count n into a two-outcome qubit measurement where $|\uparrow\rangle$ is nominally identified with $n > n_o$ and $|\downarrow\rangle$ with $n \leqslant n_o$. The optimal discriminator level that minimizes overall detection error is found to be $n_o = 1$,

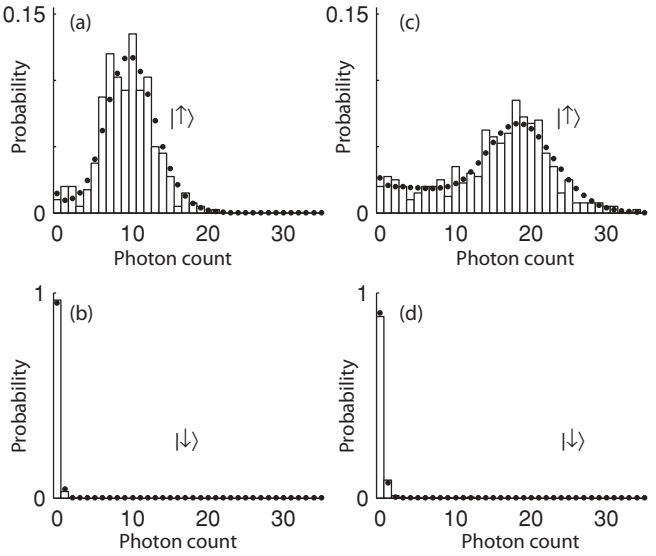

FIG. 14. Histograms of photon counts for a $^{171}Yb^{+}$ ion initially prepared in the "bright" $|\uparrow\rangle$ state or "dark" $|\downarrow\rangle$ state at two different detection laser powers, [(a) and (b)] 2.23 μW and [(c) and (d)] 8.54 μW, corresponding to a saturation parameter s_0 of 2.2 and 8.6 respectively. [(a) and (b)] For near-optimal power and best detection fidelity; [(c) and (d)] at a power larger than optimal. Other parameters are Zeeman splitting $\delta_B/2\pi = 8.19$ MHz, laser detuning -4.1 MHz, laser polarization $\theta_{BE} = 57.4^{\circ}$, detection time 0.4 ms, and photon collection efficiency $\eta = 2.9 \times 10^{-3}$. Bars are experimental data. Circles are a theoretical prediction with no free parameters that incorporates separate measurements of $|\uparrow\rangle$ preparation fidelity, and bright-state leakage rate and background count rate as functions of detection laser power.

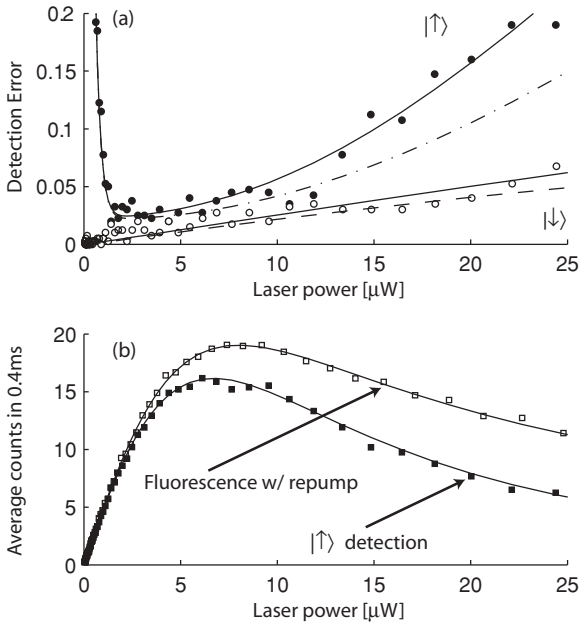

FIG. 15. $^{171}Yb^{+}$ hyperfine-qubit detection error. (a) Measured detection error of "bright" $|\uparrow\rangle$ state (solid circles) and "dark" $|\downarrow\rangle$ state (open circles) obtained from 400 repeated experiments. Parameters are the same as in Fig. 14. Discriminator is set to optimal value $n_o = 1$ ($|\uparrow\rangle$ is nominally identified with $n > n_o$ and $|\downarrow\rangle$ with $n \leqslant n_o$). The solid lines are a theoretical prediction with no free parameters that incorporates measured $|\uparrow\rangle$ preparation fidelity and measurements of bright-state leakage rate and background count rate as functions of detection laser power. The dashed line is ideal prediction for $|\downarrow\rangle$ detection ignoring background counts. The dash-dot line is ideal prediction for $|\uparrow\rangle$ detection using *calculated* bright-state leakage rate from Eq. (11). (b) The solid squares are average counts during 0.4 ms detection of $|\uparrow\rangle$ shown in (a). The superimposed line is fluorescence theory, including effect of measured bright state leakage rate. For comparison, open squares show steady-state fluorescence counts with hyperfine repump activated, similar to those in Fig. 8. The count values have been scaled to match 0.4-ms detection time and power axis has been scaled by factor 1.28 to account for loss of power to repump sidebands. Value of p_{sat} for curves shown is 0.99 μW.

limited by background counts in this case. At $n_o = 1$, the detection error for both states is calculated and shown in Fig. 15 as a function of detection laser power. Optimum detection fidelity exceeds 97% (error <0.03), which is on par with previously reported results for ytterbium [8], and is achieved over a range of laser power of ~1.5–5 μW, corresponding to $s_0 \approx 1.5$–5.

To model the measured photon counting distributions and detection fidelities, we have modified the ideal theory of Eqs. (11)–(15) in the three following ways: (i) A correction is made for $|\uparrow\rangle$-state preparation fidelity estimated to be 0.994. (ii) The background count rate is measured as a function of laser power and included in the theory of detection fidelity for the dark $|\downarrow\rangle$ state [Eq. (15)]. (iii) The leakage rate during detection of the $|\uparrow\rangle$ state has been measured as a function of laser power in a separate experiment and used in lieu of the ideal calculated rate [Eq. (11)]. The measured rate matches the ideal value at low detection powers but increases to a value 1.7 times larger than expected at high-detection laser powers. The source of the excess leakage has not been identified but may be due to nonideal diode laser spectrum, including that of the 935-nm repump laser.

The modified theory with no free parameters provides reasonable agreement with the shape of the photon count distributions (Fig. 14) and reasonable agreement with the detection errors for both qubit states (Fig. 15). The error in $|\downarrow\rangle$ detection is underestimated at lower laser powers, which may indicate a non-negligible initialization error due to incomplete optical pumping. To show the effect of the technical modifications made to the theory, figure 15 also includes the theory for $|\uparrow\rangle$ detection error using the ideal bright-state leakage rate of Eq. (11) and the theory for $|\downarrow\rangle$ detection error ignoring background counts. The excess bright-state leakage is negligible in the region of best detection fidelity. The effect of background counts is also small in the same region but only because of the chosen discriminator value $n_o = 1$. For $n_o = 0$, the $|\downarrow\rangle$ detection error exceeds 0.05.

Figure 15(b) shows the average count rate for the $|\uparrow\rangle$ state during detection. Also shown for comparison is the average count rate for steady-state fluorescence with the UV hyperfine repump activated (similar to Fig. 8). The difference between the two is well accounted for by the measured bright-state leakage rate, as can be seen from the theoretical predictions included in Fig. 15(b). Moreover, the optimum detection

fidelity is obtained at a laser power that is in the linear, low-power regime below the onset of coherent population trapping. The optimum also occurs at the average count rate of about 10 photons where the Poissonian distribution is well separated from the zero counts.

The basic behavior shown here is a reasonably optimized one at the fixed magnetic field considered. The detection time has been reduced as much as possible, and the laser power increased, to obtain fast readout and to suppress laser-independent background counts. The detection time cannot be decreased much further without compromising the fidelity; higher laser power would enter the nonlinear regime where the effective linewidth Γ_{171} is broadened [Eq. (13)] and the fluorescence is suppressed.

Further improvement of the detection fidelity requires suppression of the background counts, in particular laser scatter from the trap electrodes. In the ideal limit of no background counts, a spontaneous-emission limited fidelity of 99.3% is expected for our photon collection efficiency of 3×10^{-3} (see also Ref. [8]). Boosting the collection efficiency by a factor of ten to 3×10^{-2} would decrease the detection error by the same factor, giving a fidelity of 99.93%. This begins to approach values required by error correction models to achieve fault tolerance [41], but higher fidelities are desirable to limit resource overhead. Currently, the highest detection fidelity demonstrated for a trapped-ion qubit exceeds 99.99%, achieved for $^{40}Ca^+$ optical qubits with a collection efficiency of only 2×10^{-3} [42,43] (and an extension of this technique has realized 99.8% fidelity for the $^{43}Ca^+$ hyperfine qubit [42]). Further enhancing the fidelity of the existing detection scheme for the $^{171}Yb^+$ hyperfine qubit to these and higher levels may be possible through techniques that make use of ancilla ion-qubits [44,45] as long as sufficiently high-fidelity logic operations are available.

V. DISCUSSION AND CONCLUSION

In the previous sections, the fluorescence behavior of $^{171}Yb^+$ has been measured over a range of magnetic fields and the qubit detection was assessed at a magnetic field of ~6 G equivalent to a Zeeman shift of 8.2 MHz. There is, though, the basic question what might be an optimum magnetic field to use for quantum information applications. As far as Doppler laser cooling is concerned, a low cooling limit is important for providing a good initial condition for subsequent ground-state cooling. Berkeland and Boshier [20] point out that a magnetic field of about $\delta_B \sim \gamma/3$ provides enough fluorescence to maintain a reasonable cooling rate at peak fluorescence but does not broaden the linewidth significantly and thereby compromise the Doppler limit. This imposes a restrictive limitation on the choice of magnetic field value; nevertheless, there are the following additional considerations. For long qubit coherence times, as low a magnetic field as possible is preferred since the clock-state hyperfine qubit in $^{171}Yb^+$ is first-order insensitive to field fluctuations at zero magnetic field only. For detection fidelity and speed, the highest fluorescence count rate for the same laser power is desired, which tends to favor a larger magnetic field to suppress coherent population trapping. In fact, as long as photon collection efficiency is high enough, lower magnetic fields can be used to achieve good detection fidelity with the lower limit being the magnetic field that still gives about 10 counts on average for the bright qubit state in the detection time. Given a fixed collection efficiency η, the lowest magnetic field consistent with this limit can be estimated from Eq. (6) as $\delta_B t_d \approx (10\sqrt{6})/(\eta)$, assuming resonant detection $\Delta = 0$ and small magnetic field $\delta_B \ll \gamma$. For our case of $\eta = 3 \times 10^{-3}$ and $t_d = 0.4$ ms, the minimum field is about 2.5 G ($\delta_B/2\pi \sim 3.5$ MHz), which is within a factor of 2 of the value used for the fidelity results in Sec. IV H. Because of the appearance of the product $\delta_B t_d$, increasing the photon collection efficiency can be used either to improve the detection speed or to reduce the magnetic field and sensitivity to its fluctuations. However, given the strong constraint that efficient Doppler cooling imposes on the magnetic field value, a higher collection efficiency is largely useful for improving detection speed and fidelity only (as already detailed in Sec. IV H).

In practice, we find that it is inconvenient to operate at magnetic fields below about 3 G because the ion tends to heat and delocalize more often in the trap, presumably due to an insufficient Doppler cooling rate. A magnetic field of ~6 G ($\delta_B/2\pi = 8.2$ MHz), used in many of the results discussed above, proves to be a robust operating point. The limit for the Doppler cooling should be suitable to initiate Raman cooling in a slightly stronger trap than the one used here. At 6 G, we have measured qubit coherence for a single trapped ion that shows negligible decay out to 100 ms. Few-second coherence times have also been demonstrated for $^{171}Yb^+$ in a similar setup [8].

In conclusion, we have measured the fluorescence of a single trapped $^{171}Yb^+$ ion, which exhibits coherent population trapping in the transitions used for fluorescence detection and cooling, and we have verified a model for suppressing dark-state formation using a magnetic field of sufficient strength. We have also compared the $^{171}Yb^+$ behavior against a control isotope $^{174}Yb^+$ with simple atomic structure for which coherent population trapping is absent on the primary transition. The fluorescence behavior of the two isotopes and comparison to analytical models provide a useful means to optimize experimental parameters in preparation for quantum information applications. For $^{171}Yb^+$ in particular, measurement of fluorescence as a function of laser power and the identification of the power for peak fluorescence are a critical calibration integrated into daily experiment routine. As an application of our fluorescence studies, we have studied the fidelity of state-selective detection for the $^{171}Yb^+$ hyperfine qubit. We have obtained reasonable experimental agreement with theoretical models modified for experimental calibrations of parameters and have highlighted the role of coherent population trapping in the optimization of detection.

ACKNOWLEDGMENTS

This work is supported by NSERC and the CFI LOF program.

[1] N. Yu and L. Maleki, Phys. Rev. A **61**, 022507 (2000).
[2] C. Tamm, D. Engelke, and V. Bühner, Phys. Rev. A **61**, 053405 (2000).
[3] T. Schneider, E. Peik, and C. Tamm, Phys. Rev. Lett. **94**, 230801 (2005).
[4] K. Hosaka, S. A. Webster, A. Stannard, B. R. Walton, H. S. Margolis, and P. Gill, Phys. Rev. A **79**, 033403 (2009).
[5] J. I. Cirac and P. Zoller, Phys. Rev. Lett. **74**, 4091 (1995).
[6] D. J. Wineland, C. Monroe, W. M. Itano, D. Leibfried, B. E. King, and D. M. Meekhof, J. Res. Natl. Inst. Stand. Technol. **103**, 259 (1998).
[7] C. Balzer, A. Braun, T. Hannemann, C. Paape, M. Ettler, W. Neuhauser, and C. Wunderlich, Phys. Rev. A **73**, 041407 (2006).
[8] S. Olmschenk, K. C. Younge, D. L. Moehring, D. N. Matsukevich, P. Maunz, and C. Monroe, Phys. Rev. A **76**, 052314 (2007).
[9] A. T. Grier, M. Cetina, F. Orucevic, and V. Vuletić, Phys. Rev. Lett. **102**, 223201 (2009).
[10] C. Zipkes, S. Palzer, C. Sias, and M. Kohl, Nature (London) **464**, 388 (2010).
[11] D. Leibfried, R. Blatt, C. Monroe, and D. Wineland, Rev. Mod. Phys. **75**, 281 (2003).
[12] B. B. Blinov, D. Leibfried, C. Monroe, and D. J. Wineland, Quantum Inf. Proc. **3**, 45 (2004).
[13] M. Acton, K. A. Brickman, P. C. Haljan, P. J. Lee, L. Deslauriers, and C. Monroe, Quantum Inf. Comput. **6**, 465 (2006).
[14] E. Arimondo and G. Orriols, Lett. Nuovo Cimento **17**, 333 (1976).
[15] H. R. Gray, R. M. Whitley, and J. C. R. Stroud, Opt. Lett. **3**, 218 (1978).
[16] K.-J. Boller, A. Imamoglu, and S. E. Harris, Phys. Rev. Lett. **66**, 2593 (1991).
[17] A. Aspect, E. Arimondo, R. Kaiser, N. Vansteenkiste, and C. Cohen-Tannoudji, Phys. Rev. Lett. **61**, 826 (1988).
[18] C. F. Roos, D. Leibfried, A. Mundt, F. Schmidt-Kaler, J. Eschner, and R. Blatt, Phys. Rev. Lett. **85**, 5547 (2000).
[19] G. P. Barwood, P. Gill, G. Huang, H. A. Klein, and W. R. C. Rowley, Opt. Commun. **151**, 50 (1998).
[20] D. J. Berkeland and M. G. Boshier, Phys. Rev. A **65**, 033413 (2002).
[21] D. J. Berkeland, J. D. Miller, J. C. Bergquist, W. M. Itano, and D. J. Wineland, Phys. Rev. Lett. **80**, 2089 (1998).
[22] G. Janik, W. Nagourney, and H. Dehmelt, J. Opt. Soc. Am. B **2**, 1251 (1985).
[23] A. A. Madej and J. D. Sankey, Opt. Lett. **15**, 634 (1990).
[24] G. P. Barwood, P. Gill, G. Huang, H. A. Klein, and W. R. C. Rowley, Appl. Phys. B **61**, 385 (1995).
[25] S. Olmschenk, D. Hayes, D. N. Matsukevich, P. Maunz, D. L. Moehring, K. C. Younge, and C. Monroe, Phys. Rev. A **80**, 022502 (2009).
[26] E. H. Pinnington, G. Rieger, and J. A. Kernahan, Phys. Rev. A **56**, 2421 (1997).
[27] R. W. Berends, E. H. Pinnington, B. Guo, and Q. Ji, J. Phys. B: Atom. Mol. Phys. **26**, L701 (1993).
[28] E. Biemont, J.-F. Dutrieux, I. Martin, and P. Quinet, J. Phys. B: Atom. Mol. Phys. **31**, 3321 (1998).
[29] C. Gerz, J. Roths, F. Vedel, and G. Werth, Z. Phys. D **8**, 235 (1987).
[30] H. Lehmitz, J. Hattendorf-Ledwoch, R. Blatt, and H. Harde, Phys. Rev. Lett. **62**, 2108 (1989).
[31] A. Bauch, D. Schnier, and C. Tamm, J. Mod. Opt. **39**, 0950 (1992).
[32] M. M. Schauer, J. R. Danielson, A.-T. Nguyen, L.-B. Wang, X. Zhao, and J. R. Torgerson, Phys. Rev. A **79**, 062705 (2009).
[33] S. Chang and V. Minogin, Phys. Rep. **365**, 65 (2002).
[34] This is exactly true if instead δ_B is optimized at fixed laser power.
[35] $R(78)1-11$ absorption line in molecular iodine's $B-X$ band. See, S. Gerstenkorn, J. Verges, and J. Chevillard, *Atlas du Spectre d'Absorption de la Molecule d'Iode*, 11000–14000 cm^{-1} (Laboratoire Aime-Cotton, CNRS II, 91405 Orsay, France, 1982).
[36] W. Nagourney, G. Janik, and H. Dehmelt, Proc. Natl. Acad. Sci. USA **80**, 643 (1983).
[37] The lock offset frequency includes a 80-MHz/2 shift from the saturation setup. The wavelength quoted is corrected for an 80-MHz AOM shift in the UV.
[38] D. J. Larson, J. C. Bergquist, J. J. Bollinger, W. M. Itano, and D. J. Wineland, Phys. Rev. Lett. **57**, 70 (1986).
[39] B. B. Blinov, L. Deslauriers, P. Lee, M. J. Madsen, R. Miller, and C. Monroe, Phys. Rev. A **65**, 040304 (2002).
[40] T. Haslwanter, H. Ritsch, J. Cooper, and P. Zoller, Phys. Rev. A **38**, 5652 (1988).
[41] E. Knill, Nature (London) **434**, 39 (2005).
[42] A. H. Myerson, D. J. Szwer, S. C. Webster, D. T. C. Allcock, M. J. Curtis, G. Imreh, J. A. Sherman, D. N. Stacey, A. M. Steane, and D. M. Lucas, Phys. Rev. Lett. **100**, 200502 (2008).
[43] A. H. Burrell, D. J. Szwer, S. C. Webster, and D. M. Lucas, Phys. Rev. A **81**, 040302 (2010).
[44] T. Schaetz, M. D. Barrett, D. Leibfried, J. Britton, J. Chiaverini, W. M. Itano, J. D. Jost, E. Knill, C. Langer, and D. J. Wineland, Phys. Rev. Lett. **94**, 010501 (2005).
[45] D. B. Hume, T. Rosenband, and D. J. Wineland, Phys. Rev. Lett. **99**, 120502 (2007).